

ConsistentRFT: Reducing Visual Hallucinations in Flow-based Reinforcement Fine-Tuning

Xiaofeng Tan^{1,3,†,*} Jun Liu^{3,†} Yuanting Fan³ Bin-Bin Gao³ Xi Jiang²
 Xiaochen Chen³ Jinlong Peng³ Chengjie Wang³ Hongsong Wang^{1,‡} Feng Zheng^{2,‡}
¹Southeast University ²Southern University of Science and Technology ³Tencent YouTu Lab

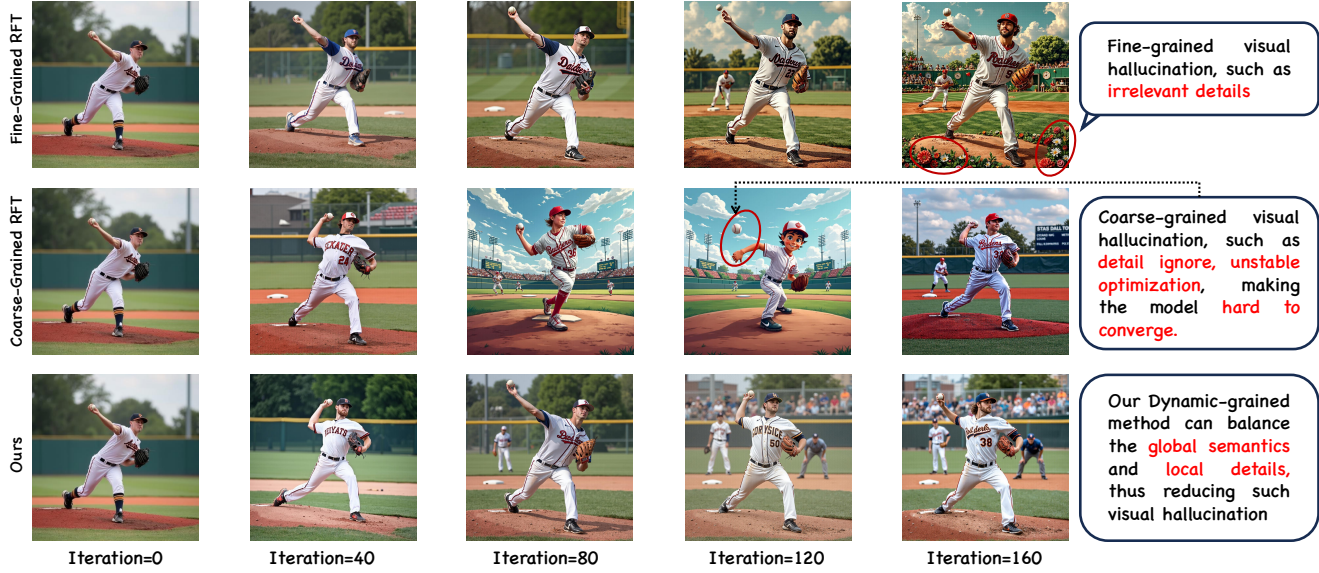


Figure 1. The optimization process of existing flow-based RFT methods. We observe that existing methods only perform fine- or coarse-grained optimization, leading to visual hallucinations. *Prompt: “A baseball player pitching a baseball on a field.”*

Abstract

Reinforcement Fine-Tuning (RFT) on flow-based models is crucial for preference alignment. However, they often introduce visual hallucinations like over-optimized details and semantic misalignment. This work preliminarily explores why visual hallucinations arise and how to reduce them. We first investigate RFT methods from a unified perspective, and reveal the core problems stemming from two aspects, exploration and exploitation: (1) limited exploration during stochastic differential equation (SDE) rollouts, leading to an over-emphasis on local details at the expense of global semantics, and (2) trajectory imitation process inherent in policy gradient methods, distorting the model’s foundational vector field and its cross-step consistency. Building on this, we propose ConsistentRFT, a general framework to mitigate these hallucinations. Specifically, we design a Dynamic Granularity Rollout (DGR) mechanism to balance

exploration between global semantics and local details by dynamically scheduling different noise sources. We then introduce a Consistent Policy Gradient Optimization (CPGO) that preserves the model’s consistency by aligning the current policy with a more stable prior. Extensive experiments demonstrate that ConsistentRFT significantly mitigates visual hallucinations, achieving average reductions of 49% for low-level and 38% for high-level perceptual hallucinations. Furthermore, ConsistentRFT outperforms other RFT methods on out-of-domain metrics, showing an improvement of 5.1% (v.s. the baseline’s decrease of -0.4%) over FLUX1.dev. This is [Project Page](#).

1. Introduction

Flow matching [14, 37] models are prominent across image [33], video [32], and robot manipulation [76], yet often lack semantic or spatial understanding [43, 52]. Reinforcement Fine-Tuning (RFT) [15, 56, 72] effectively aligns diffusion models with complex semantic objectives [34] using exter-

*Work done during Xiaofeng Tan’s internship at Tencent YouTu Lab.

†Equal contribution, ‡ Corresponding authors

Prompts: A sci-fi machine shop in a shipping container, depicted in a manga-style digital painting with intricate details. (Author's note: Prompt contains no reference to "human.")

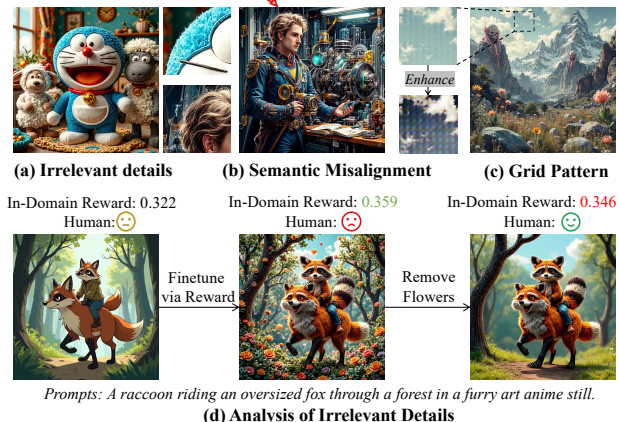


Figure 2. Visual hallucinations in flow-based reinforcement fine-tuning. We observe that (d) existing methods may learn a shortcut: boosting in-domain reward by injecting irrelevant details. We attribute this to a constrained exploration domain, discussed in Sec. 4. See Fig. S10 for clearer over-optimization details.

nal reward models [65]. To relax the deterministic ODE sampling in flow models [24, 33, 38], recent work [35, 69] explores RFT by recasting sampling as an SDE [13, 49].

Despite their successes, these methods [17, 20, 30, 31, 57, 58, 74, 81] often struggle to generate consistent, realistic images due to *visual hallucination* (see Fig. 2). This manifests as: (1) detail over-optimization [78], including irrelevant details, over-sharpening, and grid artifacts [69, 70]; (2) semantic misalignment with the prompt; and (3) cross-step inconsistency, characterized by semantic degradation and noticeable divergence under few-step sampling (see Fig. 7). Together, these issues limit the quality and reliability of current methods, particularly in out-of-domain evaluation.

Although hallucinations have been extensively studied in large language models (LLMs) [23, 79], research on visual hallucinations remains limited. Prior works [2, 16, 26, 40] primarily examine pretraining-phase hallucinations, which may arise from inappropriate smoothing of training data. In contrast to pretraining, reinforcement fine-tuning (RFT) operates without real-image data, rendering such explanations insufficient. This raises a central yet underexplored question: *Why does reinforcement fine-tuning lead to, and even exacerbate, visual hallucinations in flow-based models?*

Contributions. In this work, we aim to mitigate visual hallucinations in flow-based models. To this end, we first analyze its potential causes and subsequently propose Semantic-Consistent Reinforcement Fine-Tuning (ConsistentRFT), a general framework designed for online RFT methods, including DDPO-, DPO-, and GRPO-like methods [6, 56, 69]. Our contributions are highlighted below.

Our first contribution is to analyze why visual hallucinations arise, focusing on two RL design choices: *exploration* and *exploitation*.

(1) Exploration: SDE rollouts yield a limited exploration domain and predominantly fine-grained preference feedback, which over-optimizes local details while neglecting global semantics. **(2) Exploitation:** We reinterpret flow-based policy-gradient methods (DDPO, GRPO, DPO) as reward-weighted imitation of SDE-sampled trajectories, which distorts the consistent flow-matching vector field. This motivates *how to reduce visual hallucinations in RFT methods*.

Building on this insight, we introduce Dynamic Granularity Rollout (DGR), which balances preference signals between global semantics and local details. DGR comprises inter-group and intra-group schedules. In the inter-group schedule, we steer the model toward fine- or coarse-grained optimization via dynamic exploration: progressive noise for fine-grained rollouts and initial noise for coarse-grained rollouts. In the intra-group schedule, we adopt a progress-aware rollout with clustering to maintain diversity while reducing computation. Together, these designs balance global and local information and mitigate detail over-optimization.

Third, we propose Consistent Policy Gradient Optimization (CPGO) for policy gradient methods (DPO, DDPO, GRPO) to mitigate inconsistencies arising from trajectory imitation. CPGO preserves flow-model consistency by maintaining single-step prediction fidelity: it aligns the current model's prediction at step t with the old model's prediction at step $(t-1)$. This constraint enables imitation of high-reward trajectories while retaining consistency.

Finally, we introduce a Visual Hallucination Evaluator (VH-Evaluator) to assess detail over-optimization and perceptual hallucinations. Extensive experiments demonstrate that our method achieves superior performance over state-of-the-art (SoTA) baselines. ConsistentRFT reduces low-level artifacts by 49% and high-level hallucinations by 38%, and improves out-of-domain comprehension on FLUX1.dev by +5.1% (vs. -0.4% for the baseline), while seamlessly integrating with DDPO and DPO.

2. Related Work

Flow-based Model. Flow matching [33, 37] provides a robust generative modeling paradigm by learning continuous normalizing flows that map a simple prior to a complex data distribution. Recent advances have scaled these models to large-scale text-to-image (T2I) synthesis [7, 14, 28, 32, 42, 54, 63], demonstrating strong performance across generative tasks. Nevertheless, despite these pre-training successes, systematic post-training, e.g., preference alignment, remains insufficiently explored.

RFT in Flow-based Model. RFT aligns generative models with human preferences [34], semantic [51, 53, 61], or safety [51]. Early work [6, 15, 56, 72] introduced policy-gradient methods (DDPO, DPOK, DPO) to fine-tune diffu-

sion models with reward signals [6, 15, 56, 72]. For flow-based models, recent methods such as DanceGRPO [69] and Flow-GRPO [35] convert deterministic ODE sampling into stochastic SDE rollouts, enabling tractable likelihood estimation. Building on this, concurrent studies advance RFT along several aspects [17, 20, 30, 31, 46, 57, 58, 74, 80, 81], for example, mixed ODE-SDE sampling, pairwise preference learning, and structured trajectory sampling. Related techniques also extend to AR-based generation [75, 77] and world models [73]. Further discussion is provided in App. C. Despite this progress, visual hallucinations persist. We conduct a preliminary analysis of their causes and introduce methods to mitigate them.

3. Preliminaries: Unified Perspective on RFT

To understand why visual hallucinations arise, we first establish a unified perspective on existing RFT methods.

3.1. Unified Paradigm: Exploration & Exploitation

RFT adapts a pretrained generative model using reward feedback. Given a pretrained flow model θ , a condition dataset (e.g., prompts in T2I) $\mathcal{D} = \{c_i\}$, and a reward function $r(\mathbf{x}, c)$, RFT seeks parameters θ' that maximize the reward $r(\mathbf{x}, c)$ for samples \mathbf{x} conditioned on c . Existing methods typically follow two stages: (1) *Exploration*: generate samples with the pretrained model on conditions from \mathcal{D} and evaluate them using r ; (2) *Exploitation*: update the model using the collected rewards under a specific optimization objective. We describe these two stages below.

Exploration. Given a flow model θ and a dataset \mathcal{D} , the exploration stage is defined as:

$$\mathcal{G} = \{\mathbf{x}_0^k, \dots, \mathbf{x}_{T-1}^k, \mathbf{x}_T^k\}_{i=1}^K = \pi_\theta(c, K), \quad (1)$$

where \mathbf{x}_t^k denotes the k -th noised sample of the t -th step, K is the number of sampled trajectories, T denotes the number of sample steps, and π denotes an ODE- or SDE-based sampler (e.g., DDIM [48], DDPM [21]).

To illustrate the sampling process, we introduce the SDE formulation in DanceGRPO [69]:

$$\begin{cases} d\mathbf{x}_t = \left(\mathbf{v}_t - \frac{1}{2}\varepsilon_t^2 \nabla \log p_t(\mathbf{x}_t)\right) dt + \varepsilon_t d\mathbf{w}_t, \\ \mathbf{x}_0 = \mathbf{x}_T - \int_0^T \left(\mathbf{v}_t - \frac{1}{2}\varepsilon_t^2 \nabla \log p_t(\mathbf{x}_t)\right) dt + \int_0^T \varepsilon_t d\mathbf{w}_t. \end{cases} \quad (2)$$

where $\mathbf{v}_t = v_\theta(\mathbf{x}_t, t)$ is the model's predicted velocity and ε_t is the noise schedule. The score term is given by $\nabla \log p_t(\mathbf{x}_t) = (\mathbf{x}_t - (1-t) \cdot \hat{\mathbf{x}}_0) / t^2$, where $\hat{\mathbf{x}}_0 = \mathbf{x}_t - t \cdot \mathbf{v}_t$ is the clean sample from single-step prediction.

Exploitation. Given a flow model θ , K rollout samples with rewards $\{\mathcal{G}, r(\mathcal{G})\}$, exploitation stage aims to optimize their corresponding objective function $\mathcal{J}(\theta; \mathcal{G}, r(\mathcal{G}))$.

3.2. Representative Methods

DPO. Online DPO [8, 25, 29] is a preference-based alignment method. In the exploration stage, it draws two can-

didates per condition via Eq. (1) (i.e., $K = 2$). In the exploitation stage, it maximizes the preference margin relative with constraint from a frozen reference model θ_{ref} :

$$\mathcal{J}_{\text{DPO}}(\theta, \mathcal{G}) = \mathbb{E}_{c \sim \mathcal{D}, \mathbf{x}^1 \succ \mathbf{x}^2, t \sim \mathcal{U}(0, T)} \left[\log \sigma \left(\beta \log \left(\frac{p_\theta(\mathbf{x}_t^1 | \mathbf{x}_{t-1}^1, c)}{p_{\theta_{\text{ref}}}(\mathbf{x}_t^1 | \mathbf{x}_{t-1}^1, c)} - \frac{p_\theta(\mathbf{x}_t^2 | \mathbf{x}_{t-1}^2, c)}{p_{\theta_{\text{ref}}}(\mathbf{x}_t^2 | \mathbf{x}_{t-1}^2, c)} \right) \right) \right],$$

where $\sigma(z) = \frac{1}{1+e^{-z}}$ and $\beta > 0$ is a temperature parameter.

DDPO. As a classical RL method, DDPO [6, 15] optimizes the generative model via policy gradients using K rollouts sampled by Eq. (1), denoted as:

$$\begin{aligned} \nabla_\theta \mathcal{J}_{\text{DDPO}}(\theta, \mathcal{G}) &= \mathbb{E}_{c \sim \mathcal{D}, \mathbf{x}^{1:K}, t \sim \mathcal{U}(0, T), k \sim \mathcal{U}(1, K)} \\ &\quad \nabla_\theta \left[r(\mathbf{x}_0^k, c) \cdot \log p_\theta(\mathbf{x}_t^k | \mathbf{x}_{t-1}^k, c) \right]. \end{aligned} \quad (3)$$

GRPO. By estimating advantages \mathcal{A}^k by a group of K rollouts, GRPO [19] optimizes a clipped surrogate:

$$\begin{aligned} \mathcal{J}_{\text{GRPO}}(\theta, \mathcal{G}) &= \mathbb{E}_{c \sim \mathcal{D}, \mathbf{x}^{1:K}, t \sim \mathcal{U}(0, T), k \sim \mathcal{U}(1, K)} \\ &\quad \left[\min(\rho_\theta^{k,t} \mathcal{A}^k, \text{clip}(\rho_\theta^{k,t}, 1 - \varepsilon, 1 + \varepsilon) \mathcal{A}^k) \right], \end{aligned} \quad (4)$$

where advantages \mathcal{A}^k and $\rho_\theta^{k,t}$ are computed as follows:

$$\mathcal{A}^k = \frac{r(\mathbf{x}_0^k, c) - \mu(r(\mathbf{x}^{1:K}, c))}{\sigma(r(\mathbf{x}^{1:K}, c))}, \quad \rho_\theta^{k,t} = \frac{p_\theta(\mathbf{x}_t^k | \mathbf{x}_{t-1}^k, c)}{p_{\theta_{\text{old}}}(\mathbf{x}_t^k | \mathbf{x}_{t-1}^k, c)},$$

and $\mu(r(\mathbf{x}^{1:K}, c))$ and $\sigma(r(\mathbf{x}^{1:K}, c))$ are the mean and standard deviation of the reward value of group samples $\mathbf{x}^{1:K}$.

Summary. These methods share an SDE-based exploration via rollouts but differ in their exploitation strategies. Intuitively, samples generated during exploration serve as the informational basis for exploitation, thereby shaping the model's optimization behavior. This view motivates our investigation into the causes of visual hallucinations.

4. Motivation: Why do Hallucinations Arise?

Here, we preliminarily study visual hallucinations from rollout and optimization: (i) limited rollout diversity that overemphasizes fine-grained details and neglects global semantics; and (ii) imitation of SDE-sampled trajectories that disrupts velocity consistency in flow-based models.

4.1. Exploration: Limited Exploration Domain

RFT methods optimize generative models by exploiting the variation among rollout samples and their rewards. For example, DPO constructs preference pairs and maximize their probability margin, whereas GRPO exploits group-wise discrepancies with normalized advantages to emphasize high-reward trajectories. Consequently, rollout design is a primary determinant of the optimization dynamics.

Discussion. Ideally, the model should generate rollouts that exhibit both global semantic diversity and fine-grained

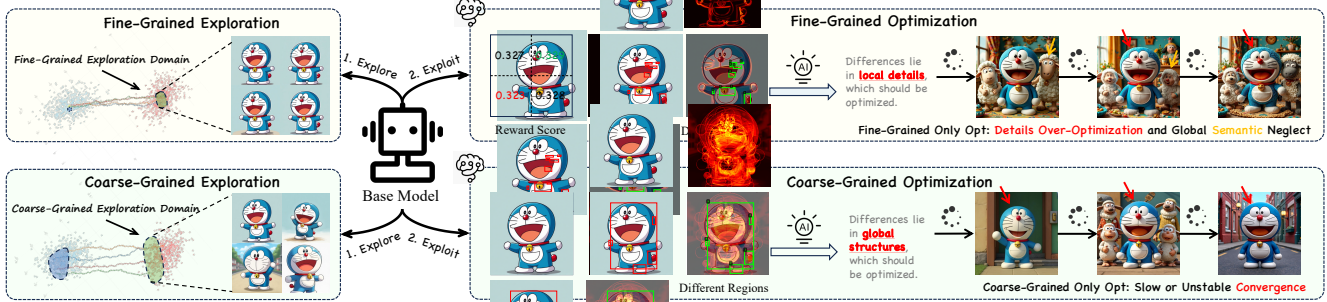


Figure 3. Relationship between exploration (rollout) and exploitation (optimization). We observe that the groups exhibiting coarse/fine-grained differences obtained during the rollout stage may steer the model toward coarse/fine-grained optimization. Ideally, the model should not focus solely on fine-grained details or on coarse-grained semantics. For more quantitative analysis, please refer to App. A.3.

variation, with reward signals that faithfully capture both. However, we observe that existing methods¹ exhibit fine-grained optimization due to the limited diversity induced solely by SDE process. As shown in Fig. 3 (see *Fine-Grained Optimization* Region), methods such as Dance-GRPO [30, 31, 69], which use the same noise initialization but varying process noise, often produce highly similar images within the same group. While this facilitates learning fine details, it ignores global semantics.

Thus, optimizing the model within such a limited exploration domain may cause the model to *suffer from overemphasizing fine-grained details while ignoring global semantics*. More importantly, reward models trained on discrete preference data [59, 68] (e.g., preferred vs. unpreferred) typically induce non-smooth response surfaces [2, 16, 26, 40]. Fine-tuning model under such fine-grained feedback risks model failing to the local optima that exhibit high reward-value but poor visual quality (See Fig. 3 *Fine-Grained Optimization* Region).

4.2. Exploitation: Trajectory Imitation

To further understand the optimization objectives of RFT methods, we reinterpret them as *trajectory imitation* by analyzing their gradients. Taking GRPO as a case study, we state our main result in Corollary 1; its proof is in App. E.1. Analogous results for DDPO and DPO appear in App. E.2.

Corollary 1 (Reinterpretation of GRPO). *Given a flow model θ , a reward model $r(\mathbf{x}, c)$, and trajectories sampled via SDE in Eq. (1), the gradient of the GRPO satisfies*

$$\nabla_{\theta} \mathcal{J}_{\text{GRPO}} = \begin{cases} 0, & \text{if } (u_1 \wedge v_1) \vee (u_2 \wedge \neg v_1), \\ \nabla_{\theta} \mathbb{E} \left[-\omega(t) \cdot \mathcal{A}^k \cdot \|\mu_{\theta}(\mathbf{x}_t, t, c) - \mathbf{x}_{t-1}\|_2^2 \right], & \text{else.} \end{cases}$$

where $\mu_{\theta}(\cdot)$ denotes the mean value of predicted distribution of $p_{\theta}(\mathbf{x}_t \mid \mathbf{x}_{t-1})$, $\mathbb{I}(\cdot)$ is the indicator function, and conditions u_1 and u_2 are defined as follows:

$$u_1 \leftarrow \mathbb{I}(\rho_{t,i} \leq 1 - \epsilon), \quad u_2 \leftarrow \mathbb{I}(\rho_{t,i} \geq 1 + \epsilon), \quad v_1 \leftarrow \mathbb{I}(\mathcal{A}^k < 0).$$

¹Some works, such as Flow-GRPO, perform coarse-grained optimization for sparse rewards (e.g., object count). They are discussed in App. B.4.

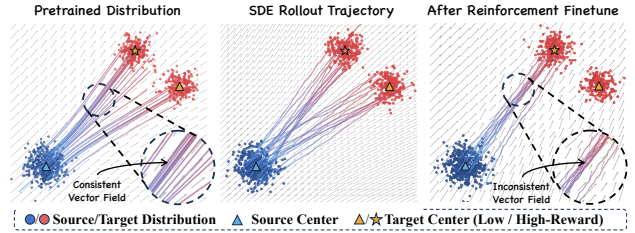


Figure 4. Toy example of trajectory imitation optimization in policy gradient methods.

Reinterpretation. Corollary 1 shows that GRPO effectively reinterpret as trajectory imitation: its optimization is equivalent, in gradient, to a reward-weighted trajectory-imitation objective. Specifically, the optimization encourages the predicted velocity field \mathbf{v}_{θ} to match the trajectory of the sampled SDE trajectory $\mu_{\theta}(\mathbf{x}_t^k) \approx \mathbf{x}_{t-1}^k$ (See blue region in Fig. 5), weighted by the advantage \mathcal{A}^k . This indicates that the model tends to imitate trajectories with high reward ($\mathcal{A}^k > 0$), while forget trajectories with low reward ($\mathcal{A}^k < 0$).

Discussion. However, this post-training objective creates a fundamental conflict with the pre-training goal. For flow models, pre-training aims to learn a consistent velocity field that defines straight, deterministic trajectories, whereas GRPO-based fine-tuning compels the model to imitate stochastic, non-linear SDE trajectories. As a toy example in Fig. 4 illustrates, this conflict disrupts the learned velocity consistency, leading to inconsistent results across different sampling steps. More importantly, uncritically imitating the results of SDE may further aggravate the hallucinations discussed above in Sec. 4.1.

5. Method: How to Reduce Hallucinations?

Here, we introduce our proposed ConsistentRFT, which comprises two core components designed to address the aforementioned causes of hallucinations. Specifically, (i) *Dynamic Granularity Rollout* targets the Limited Exploration Domain, and (ii) *Consistent Policy Gradient Opti-*

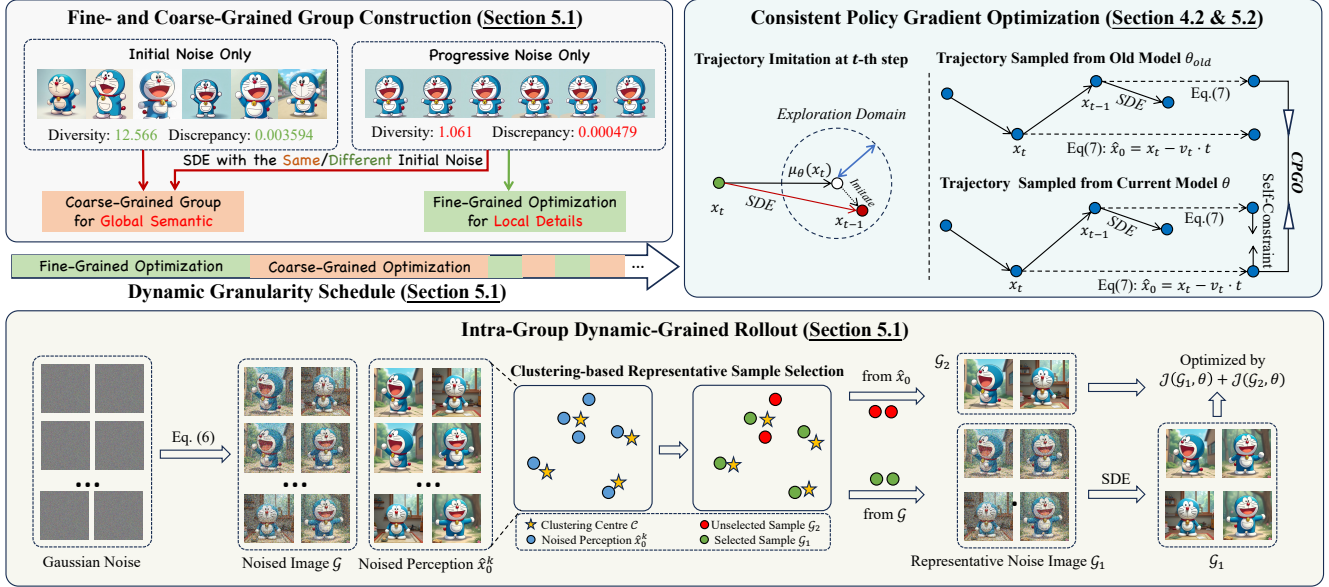


Figure 5. Overview of ConsistentRFT, consisting of (i) Dynamic Granularity Rollout, and (ii) Consistent Policy Gradient Optimization.

mization resolves the issues arising from Trajectory Imitation Optimization.

5.1. Exploration: Dynamic Granularity Rollout

To overcome the mismatch between probabilistic objectives and deterministic dynamics, existing RFT methods inject stochasticity via SDE-based samplers to obtain the likelihood. SDE in Eq. (2) indicates that rollout starts from a initialization x_T and further injects randomness via the Brownian term, yielding two sources of stochasticity: (i) the initial noise x_T , and (ii) the progressive SDE noise w_t .

Our Dynamic Granularity Rollout starts from a *key observation*: initial latent perturbations largely determine global semantics, while progressive perturbations refine local details (see Fig. 3 and Fig. 5). Quantitative validation is provided in App. A.5, consistent with observations in [4, 9, 82]. Motivated by this observation, we introduce DGR with both (1) Intra-Group and (2) Inter-Group setting. **(1) Inter-Group Dynamic-Grained Rollout.** Our goal is to enable the RFT method to perceive both global semantics and local details. Motivated by the above observation, we suggest achieving this dynamic schedule the “fine-grained” and “coarse-grained” groups to guide the model focus on such details and semantics, as shown in Fig. 3.

Fine- and Coarse-Grained Group. To obtain the fine- and coarse-grained groups, we leverage the different behavior between progressive and initial noise, as follows:

$$\{\mathbf{x}_T^k\}_{k=1}^K = \begin{cases} \{\mathbf{x}_T^k \mid \mathbf{x}_T^k \stackrel{\text{i.i.d.}}{\sim} \mathcal{N}(\mathbf{0}, \mathbf{I})\}, & \text{if Coarse-Grained,} \\ \{\mathbf{x}_T^k \mid \mathbf{x}_T^k \leftarrow (\mathbf{x}_T \sim \mathcal{N}(\mathbf{0}, \mathbf{I}))\}, & \text{else.} \end{cases} \quad (5)$$

By contrasting samples within such groups, this method enables models to perceive global semantics and local details.

Dynamic Granularity Schedule. To mitigate hallucinations from fixed-granularity optimization, we introduce the Dynamic Granularity Schedule that balances global semantics and local details, as shown in Fig. 5. For an optimization of N iterations, we partition training into N/j periods, with $j = j_g + j_c$ iterations, each comprising j_g fine-grained steps followed by j_c coarse-grained steps. This strategy balances global structure and fine-grained detail, as shown in Fig. 2.

(2) Intra-Group Dynamic-Grained Rollout. Although Inter-Group DGS enables both coarse- and fine-grained optimization, limited diversity in fine-grained groups leads to redundant computation and hallucinations. To this end, we propose Intra-Group Dynamic Granularity Rollout, which leverages the single-step prediction to coarsely assess intermediate states, enabling sample diversity enhancement.

Coarse Progress Perception. For each rollout, we first perform t_s steps of sampling from K initialized noise \mathbf{x}_T^k . We then apply a single-step sampling at the intermediate states for coarse perspectives. This procedure is given by:

$$\begin{cases} \mathbf{x}_{t_s}^k = \mathbf{x}_T^k - \int_{t_s}^T \left(\mathbf{v}_t^k - \frac{1}{2} \varepsilon_t^2 \nabla \log p_t(\mathbf{x}_t^k) \right) dt + \int_{t_s}^T \varepsilon_t \, dw_t^k, \\ \hat{\mathbf{x}}_0^k = \mathbf{x}_{t_s}^k - \mathbf{v}_{t_s}^k \cdot t_s. \end{cases} \quad (6)$$

Owing to the optimal transport in flow models, intermediate state perception at t_s highly correlates with full-sampling outcomes. Quantitative results are in App. A.4.

Cluster-Based Selection & Fine-Grained Refinement. Building on intermediate-state perception, we seek representative samples to further enhance diversity for reducing hallucinations and computation. A naïve approach is to form a new group by selecting the N highest- and lowest-reward samples; however, these selections often exhibit

high similarity (e.g., the top- N images are similar), yielding limited diversity. Thus, we adopt a clustering-based selection to obtain representative and diverse groups.

Our method (as shown in Fig. 5) initializes with K Gaussian noises. After t_s denoising steps, we obtain intermediate states $\{\hat{\mathbf{x}}_{t_s}^k\}_{k=1}^K$, which are clustered in the latent space to produce N centers \mathcal{C} ($N < K$). We then form the representative set \mathcal{G}_1 by selecting the N samples nearest to \mathcal{C} and define the remainder as \mathcal{G}_2 . Denoising is resumed for \mathcal{G}_1 to complete trajectories. This yields two subsets: \mathcal{G}_1 , representative, detail-rich, with completed trajectories, and, \mathcal{G}_2 , coarsely intermediate perception. See details in App. B.3.

By optimizing such representative groups, our rollout preserve diversity with fewer samples and offers three benefits: (i) enhanced diversity to prevents fine-grained hallucination; (ii) reduced computation by selecting a representative \mathcal{G}_1 from intermediate state; and (iii) stronger early coarse-grained optimization, as both groups capture early steps [67] and reinforce them via dual groups optimization.

5.2. Exploitation: CPGO

As discussed above, existing RFT methods can exacerbate visual hallucinations and compromise the intrinsic consistency of flow models. Hence, we propose Consistent Policy Gradient Optimization, which enforces consistency via ODE-based (rather than SDE-based) predictions.

As shown in Fig. 5, our core insight is to enforce single-step consistency via two complementary ways: (i) imitation of a model with better consistency (e.g., the old model in Eq. (2)), and (ii) temporal self-consistency (e.g., aligning results at step t with those of step $t-1$). We detail the formulation and provide theoretical justification below.

Single-Step Prediction. Flow models enable single-step prediction: clean samples can be recovered from noisy states in one-step first-order ODE Euler solver:

$$\pi_\theta^{\text{ODE}}(\mathbf{x}_t, t) : \mathbf{x}_0 = \mathbf{x}_t - t \cdot v_\theta(\mathbf{x}_t, t). \quad (7)$$

No extra overhead is incurred, as it reuses the velocity $v_\theta(\mathbf{x}_t, t)$ from SDE sampling (see App. B.2).

Consistent Policy Gradient Optimization. We enforce consistency via imitation and temporal self-consistency. A naive consistency-style formulation [50] is constrained by (i) target proximity to the current policy and (ii) reliability of teacher predictions. We therefore define:

$$\begin{aligned} \mathcal{J}_{\text{ConsistentRFT}}(\theta, \mathcal{G}) &= \mathcal{J}_{\text{GRPO}}(\theta, \mathcal{G}) + \omega \cdot \mathcal{J}_{\text{CPGO}}(\theta, \mathcal{G}) \\ \mathcal{J}_{\text{CPGO}}(\theta, \mathcal{G}) &= -\mathbb{E}_{t \in \mathcal{U}(\tau, 0)} \left[\|\pi_\theta^{\text{ODE}}(\mathbf{x}_t^k, t) - \pi_{\theta_{\text{old}}}^{\text{ODE}}(\mathbf{x}_{t-1}^k, t-1)\|_2^2 \right] \end{aligned}$$

where τ is a threshold to exclude unreliable results from high-noise samples, and ω is the weight parameter.

This method ensures stability with cross-step targets from an old policy close to the current one, and reliability by applying filtering unreliable predictions. For theoretical justification, its effectiveness is provided in App. E.3.

In summary, CPGO enhances consistency by constraining RFT along the ODE trajectory, preventing the model from imitating hallucinated samples interpolated from the pre-trained distribution [2, 16, 26, 40].

5.3. Evaluation: Visual Hallucination Evaluator

Existing benchmarks (e.g., preference [39], personalized [36, 41], compositional [18, 22]) overlook visual hallucinations, especially over-optimization. We introduce VH-Evaluator, combining objective low-level metrics with pre-trained MLLM-based high-level assessment [3]. Further discussion and the prompt appear in App. D.

6. Experiments

6.1. Experimental Setup

Datasets & Models. We adopt the HPDv2 [65] prompts for online training and evaluation under the HPS-v2 benchmark setup. Given that most post-training pipelines use fewer than $10k$ prompts, we hold out the last 400 prompts from the 103.7k training set for validation. Our main text-to-image based model is FLUX.1 dev [28]. See details in App. A.2.

Metrics. We report human preference scores (ImageReward [68], PickScore [27]), aesthetic quality [12], and semantic alignment (CLIP [44], Unified Reward [59]). We distinguish the in-domain training reward (e.g., HPS-v2.1) from out-of-domain metrics, which we prioritize to evaluate generalization. Visual hallucinations are assessed across three aspects: (i) detail over-optimization, measured by our VH-Evaluator; (ii) semantic consistency, using CLIP and Unified Reward; and (iii) trajectory consistency, evaluated by the straightness of the latent trajectory (see App. D).

Implementation. Our method is compatible with standard policy-gradient baselines. For methods finetuning FLUX with HPS (e.g., DanceGRPO [69], MixGRPO [30]), we follow official hyperparameters. Classic baselines (DPO [56], DDPO [6]) are reproduced via the DanceGRPO codebase under our setup. During rollout, we use $N_{\text{old}}=16$ steps and group size 12; Inter-Group DGS period is 40 with coarse ratio 0.25; Intra-Group DGS uses intermediate perception at step 12 with dual groups of size 6. In optimization, the CPGO weight is 10^{-6} and the threshold is $\tau = 0.6$. Additional details are in App. A.2.

6.2. Main Results

Comparison with SoTA RFT Methods. As shown in Tab. 1, existing methods often sacrifice out-of-domain performance for in-domain gains, indicating vision hallucination. For example, MixGRPO boosts HPSv2.1 by 15.7% but degrades CLIP by 10.8%, while D3PO improves HPSv2.1 by 8.3% at the cost of 2.3% CLIP drop. In contrast, our ConsistentRFT achieves superior generalization with 18.9% ImageReward and 6.2% Aesthetic improve-

Table 1. Comparison with SoTA RFT methods. Gray text denotes in-domain metrics. Best results are highlighted in **bold**.

Method	Reward	Human Preference			Aesthetic		Semantic		Comprehensive	
		HPSv2.1	ImageReward	PickScore	Aes.Pred.v2.5	CLIP	Unified Reward-S	Unified Reward	Avg.	
Flux Dev [28] (Base)	-	0.312	1.089	0.226	5.837	0.388	3.365	3.520	2.105	
<i>DDPO-Based Methods</i>										
DDPO [6]	<i>HPSv2.1</i>	<i>0.313_{+0.3%}</i>	1.129 _{+3.7%}	0.227 _{+0.4%}	5.896 _{+1.0%}	0.391 _{+0.8%}	3.387 _{+0.7%}	3.568 _{+1.4%}	2.130 _{+1.2%}	
w/ ConsistentRFT	<i>HPSv2.1</i>	<i>0.324_{+3.8%}</i>	<i>1.197_{+9.9%}</i>	<i>0.228_{+0.9%}</i>	<i>5.998_{+2.8%}</i>	<i>0.396_{+2.1%}</i>	<i>3.476_{+3.3%}</i>	<i>3.593_{+2.1%}</i>	<i>2.173_{+3.2%}</i>	
<i>DPO-Based Methods</i>										
Diffusion-DPO [56]	<i>HPSv2.1</i>	<i>0.318_{+1.9%}</i>	1.177 _{+8.1%}	0.230 _{+1.8%}	5.967 _{+2.2%}	0.393 _{+1.3%}	3.424 _{+1.8%}	3.528 _{+0.2%}	2.148 _{+2.0%}	
D3PO [72]	<i>HPSv2.1</i>	<i>0.338_{+8.3%}</i>	1.185 _{+8.8%}	0.227 _{+0.4%}	5.849 _{+0.2%}	0.379 _{-2.3%}	3.396 _{+0.9%}	3.507 _{-0.4%}	2.126 _{+1.0%}	
w/ ConsistentRFT	<i>HPSv2.1</i>	<i>0.334_{+7.1%}</i>	<i>1.249_{+14.7%}</i>	<i>0.232_{+2.7%}</i>	<i>6.077_{+4.1%}</i>	<i>0.394_{+1.5%}</i>	<i>3.499_{+4.0%}</i>	<i>3.570_{+1.4%}</i>	<i>2.194_{+4.2%}</i>	
<i>GRPO-Based Methods</i>										
DanceGRPO [69]	<i>CLIP+HPSv2.1</i>	<i>0.336_{+7.7%}</i>	1.124 _{+3.2%}	0.229 _{+1.3%}	5.746 _{-1.6%}	0.407 _{+4.9%}	3.333 _{-1.0%}	3.491 _{-0.8%}	2.095 _{-0.5%}	
w/ ConsistentRFT	<i>CLIP+HPSv2.1</i>	<i>0.329_{+5.4%}</i>	<i>1.349_{+23.9%}</i>	<i>0.235_{+4.0%}</i>	<i>6.057_{+3.8%}</i>	<i>0.401_{+3.4%}</i>	<i>3.493_{+3.8%}</i>	<i>3.612_{+2.6%}</i>	<i>2.211_{+5.0%}</i>	
MixGRPO [30]	<i>HPSv2.1</i>	<i>0.361_{+15.7%}</i>	1.201 _{+10.3%}	0.222 _{-1.8%}	5.833 _{-0.1%}	0.346 _{-10.8%}	3.293 _{-2.1%}	3.401 _{-3.4%}	2.094 _{-0.5%}	
w/ ConsistentRFT	<i>HPSv2.1</i>	<i>0.354_{+13.5%}</i>	<i>1.323_{+21.5%}</i>	<i>0.228_{+0.9%}</i>	<i>6.052_{+3.7%}</i>	<i>0.374_{-3.6%}</i>	<i>3.328_{-1.1%}</i>	<i>3.432_{-2.5%}</i>	<i>2.156_{+2.4%}</i>	
FlowGRPO [35]	<i>HPSv2.1</i>	<i>0.326_{+4.5%}</i>	1.135 _{+4.2%}	0.226	5.926 _{+1.5%}	0.375 _{-3.4%}	3.320 _{-1.3%}	3.476 _{-1.3%}	2.112 _{+0.3%}	
DanceGRPO [69]	<i>HPSv2.1</i>	<i>0.353_{+13.1%}</i>	1.155 _{+6.1%}	0.226	5.897 _{+1.0%}	0.361 _{-7.0%}	3.300 _{-1.9%}	3.379 _{-4.0%}	2.096 _{-0.4%}	
PrefGRPO [58]	<i>HPSv2.1</i>	0.340 _{+10.9%}	1.172 _{+7.6%}	0.227 _{+0.4%}	5.953 _{+2.0%}	0.378 _{-2.6%}	3.338 _{-0.8%}	3.486 _{-1.0%}	2.129 _{+1.1%}	
[69] w/ ConsistentRFT	<i>HPSv2.1</i>	0.348 _{+11.5%}	<i>1.295_{+18.9%}</i>	<i>0.230_{+1.8%}</i>	<i>6.197_{+6.2%}</i>	<i>0.384_{-1.0%}</i>	<i>3.408_{+1.3%}</i>	<i>3.622_{+2.9%}</i>	<i>2.212_{+5.1%}</i>	

Table 2. Comparison with SoTA pretrained models. Best results are in **bold**, and the second-best results are in underline.

Method	Reward	Human Preference			Aesthetic		Semantic		Comprehensive		Time (s)
		HPSv2.1	ImageReward	PickScore	Aes.Pred.v2.5	CLIP	Unified Reward-S	Unified Reward	Avg.		
SDXL [42]	-	0.292	0.945	0.226	5.735	<u>0.418</u>	3.275	3.425	1.988	9	
Hunyuan-DiT [32]	-	0.302	1.094	0.225	5.616	0.411	3.296	3.458	2.057	23	
SD-3.5-M [14]	-	0.302	1.130	0.227	5.659	0.411	3.350	3.580	2.094	14	
Kolor [54]	-	0.312	0.974	0.225	6.000	0.386	3.296	3.376	2.098	31	
SD-3.5-L [14]	-	0.303	1.143	0.228	5.853	0.410	3.330	3.627	2.128	17	
HiDream-Full [7]	-	0.325	<u>1.385</u>	<u>0.231</u>	5.742	0.412	3.407	<u>3.714</u>	2.174	75	
Qwen-Image [63]	-	0.324	1.427	0.233	6.048	0.421	3.436	3.891	2.254	128	
Flux Dev [28] (Base)	-	0.312	1.089	0.226	5.837	0.388	3.365	3.520	2.105	36	
w/ Ours	<i>HPSv2.1</i>	0.348	1.295	0.230	<u>6.197</u>	0.384	<u>3.408</u>	3.622	2.212	36	
Ours w/ 20-step sampling	<i>HPSv2.1</i>	<u>0.346</u>	1.311	0.231	6.229	0.384	3.407	3.596	<u>2.215</u>	14	

ments, confirming that our ConsistentRFT effectively balance in-domain and out-of-domain performance.

Comparison with SoTA Pretrained Model. When applied to the FLUX-Dev base model, our method achieves a strong average score of 2.212 (+5.1%) while maintaining a similar performance on the few-step setting, as detailed in Tab. 2. These results surpass other efficient models (inference time < 100s) and rival the powerful Qwen-Image model (2.254) while being 9x faster (14s vs. 128s). The significant speedup highlights the efficiency of our CPGO optimization, and the performance gains demonstrate our method’s effectiveness in mitigating visual hallucinations.

Evaluation on Vision Hallucination. We now evaluate visual hallucinations of RFT methods, with results presented in Tab. 3. The analysis confirms two key findings: (i) existing RFT methods often introduce visual hallucinations, and (ii) our method effectively mitigates these introduced hallucinations. For instance, while DanceGRPO [69] and MixGRPO [30] inflate artifact scores to 2.04 and 2.21 (from a 0.66 baseline), our ConsistentRFT reverses this degradation, reducing the scores by 38% (to 1.26) and 24% (to 1.68), respectively. These results with the user study (Fig.

8) demonstrate that our approach successfully curtails visual hallucinations, leading to reliable image generation.

Comparison with Methods for Reward Hacking. Reward hacking is closely related to visual hallucination and is likely one of the primary causes. We compare ConsistentRFT with established mitigation techniques (Tab. 3). Common techniques such as LoRA [62] and Early Stopping [10] offer limited gains: LoRA reduces artifacts by 5.4%, while Early Stopping increases them by 17%. KL divergence cuts 19% of artifacts but suppresses preference scores [69], and PrefGRPO [58] only 9.8%. By contrast, our method reduces hallucination by 38% and raises the average out-of-domain score by 5.7%, confirming its effectiveness against visual hallucinations.

6.3. Ablation Study

Fine-, Coarse-, and Dynamic-Grained Optimization. As illustrated in Fig. 1, fine-grained optimization favors local details but hurts global semantics, while coarse-grained does the opposite, revealing a clear trade-off (Tab. 4). Specifically, fine-grained yields high in-domain HPS (0.353) but low CLIP (0.361), whereas coarse-grained

Table 3. Evaluation results on visual hallucination and out-of-domain metrics.

Method	Over-Optimization (Low-Level) ↓			Over-Optimization (High-Level) ↓			Cons. ↓		Out-of-Domain Metric ↑							
	Lap. Var.	High-Freq. Edge	Noise	Sharp. Irrel. Det.	Grid Pat.	Avg.	Lat. Cons.	IR	PS	Aes.	CLIP	UR-S	UR	Avg.		
Flux Dev [28]	977	26	61	0.27	1.00	0.87	0.12	0.66	0.30	1.09	0.226	5.84	0.39	3.37	3.52	2.40
DDPO [6]	3895	68	71	0.78	2.48	2.52	0.61	1.87	0.32	1.13	0.227	5.90	0.39	3.39	3.57	2.43
w/ ConsistentRFT	1028 <small>-74%</small>	40 <small>-41.2%</small>	66 <small>-7.0%</small>	0.62 <small>-20.5%</small>	1.07	0.92	0.12	0.70 <small>-62.6%</small>	0.30	1.20	0.228	6.00	0.40	3.48	3.59	2.48 <small>+1.9%</small>
OnlineDPO [72]	2752	44	62	0.61	2.43	2.20	0.58	1.74	0.32	1.19	0.227	5.85	0.38	3.40	3.51	2.43
w/ ConsistentRFT	1131 <small>-59%</small>	37 <small>-15.9%</small>	59 <small>-4.8%</small>	0.59 <small>-3.3%</small>	1.50	1.34	0.29	1.04 <small>-40.2%</small>	0.30	1.25	0.232	6.08	0.39	3.50	3.57	2.50 <small>+3.2%</small>
MixGRPO [30]	3900	82	66	2.65	3.12	2.73	0.79	2.21	0.35	1.20	0.222	5.83	0.35	3.29	3.40	2.38
w/ ConsistentRFT	1309 <small>-66%</small>	45 <small>-45.1%</small>	53 <small>-19.7%</small>	1.17 <small>-55.8%</small>	2.43	2.08	0.54	1.68 <small>-24.0%</small>	0.31	1.32	0.228	6.05	0.37	3.33	3.43	2.46 <small>+3.4%</small>
DanceGRPO [69]	5348	91	68	2.10	2.76	2.69	0.68	2.04	0.33	1.16	0.226	5.90	0.36	3.30	3.38	2.39
w/ LoRA Scale [62]	6707 <small>+25%</small>	99 <small>+8.7%</small>	69 <small>+0.5%</small>	2.00 <small>-4.8%</small>	2.71	2.43	0.66	1.93 <small>-5.4%</small>	0.33	1.16	0.228	5.98	0.37	3.40	3.45	2.43 <small>+1.6%</small>
w/ KL [10]	3699 <small>-31%</small>	79 <small>-13.0%</small>	68 <small>-0.2%</small>	2.22 <small>+5.9%</small>	2.37	2.03	0.55	1.65 <small>-19.0%</small>	0.31	1.11	0.227	5.92	0.37	3.31	3.46	2.40 <small>+0.6%</small>
w/ Early Stop [10]	3604 <small>-33%</small>	77 <small>-15.0%</small>	65 <small>-4.2%</small>	2.29 <small>+9.3%</small>	3.16	3.17	0.83	2.39 <small>+17.0%</small>	0.32	1.09	0.225	5.92	0.36	3.29	3.38	2.38 <small>-0.4%</small>
w/ PrefGRPO [58]	2634 <small>-51%</small>	71 <small>-21.0%</small>	62 <small>-9.5%</small>	2.24 <small>+6.9%</small>	2.59	2.20	0.73	1.84 <small>-9.8%</small>	0.33	1.17	0.227	5.95	0.37	3.34	3.49	2.43 <small>+1.7%</small>
w/ ConsistentRFT	1421 <small>-73%</small>	45 <small>-50.5%</small>	57 <small>-16.2%</small>	0.93 <small>-55.7%</small>	1.81	1.59	0.37	1.26 <small>-38.2%</small>	0.30	1.30	0.230	6.20	0.38	3.41	3.62	2.52 <small>+5.4%</small>

Table 4. Ablation study of ConsistentRFT components.

Method	Granularity	Time	HPS	IR	PS	Aes.	CLIP	UR-S	UR	Avg.
Flux Dev (Base)	-	-	0.312	1.09	0.226	5.84	0.388	3.37	3.52	2.40
DanceGRPO	<i>Fine</i>	665	0.353	1.16	0.226	5.90	0.361	3.30	3.38	2.39
-	<i>Coarse</i>	665	0.326	1.14	0.226	5.93	0.375	3.32	3.48	2.41
+ Inter DGR	<i>Dynamic</i>	665	0.349	1.19	0.230	6.14	0.376	3.35	3.50	2.46
+ CPGO	<i>Dynamic</i>	665	0.348	1.30	0.230	6.20	0.384	3.41	3.62	2.52
+ Intra DGR	<i>Dynamic</i>	541	0.348	1.28	0.231	6.16	0.373	3.39	3.53	2.49
OnlineDPO	<i>Coarse</i>	373	0.338	1.19	0.227	5.85	0.379	3.40	3.51	2.42
-	<i>Fine</i>	373	0.340	1.15	0.228	5.92	0.374	3.38	3.44	2.42
+ Inter DGR	<i>Dynamic</i>	373	0.322	1.19	0.228	6.00	0.392	3.42	3.52	2.46
+ CPGO	<i>Dynamic</i>	373	0.334	1.25	0.232	6.08	0.394	3.50	3.57	2.50
DDPO	<i>Fine</i>	665	0.313	1.13	0.227	5.90	0.391	3.39	3.57	2.43
-	<i>Coarse</i>	665	0.309	1.11	0.226	5.91	0.389	3.37	3.57	2.43
+ Inter DGR	<i>Dynamic</i>	665	0.316	1.15	0.228	5.95	0.392	3.41	3.59	2.45
+ CPGO	<i>Dynamic</i>	665	0.324	1.20	0.228	6.00	0.396	3.48	3.59	2.48
+ Intra DGR	<i>Dynamic</i>	541	0.322	1.18	0.228	5.95	0.401	3.50	3.57	2.47

flips this (0.326 HPS, 0.375 CLIP). Our DGR resolves this trade-off, attaining competitive HPS (0.349) and CLIP (0.376) by balancing local details and global semantics.

Effectiveness of CPGO. CPGO enhances internal consistency, raising the average out-of-domain score to 2.523 and ImageReward by 9.2% (Tab. 4). We attribute these gains to constrained interpolation within smoother distributions [2]. CPGO also sustains quality under few-step sampling where DanceGRPO degrades (Fig. 7(a)). Notably, 20-step sampling (2.215) slightly surpasses the full-step result (2.212) in Tab. 1, indicating improved vector-field consistency across steps. Overall, CPGO improves reliability and fidelity by enforcing consistency for efficient generation.

Effectiveness of Intra-Group DGS. Intra-group DGS uses intermediate perception to preserve diversity while accelerating fine-tuning: it reduces DanceGRPO training time

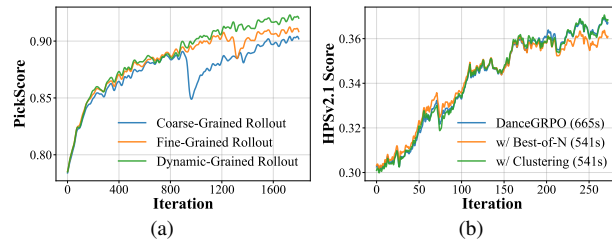


Figure 6. Reward curves. (a) reward curve over training iterations with FlowGRPO trained using PickScore; (b) reward curve over training iterations with DanceGRPO trained using HPSv2.1.

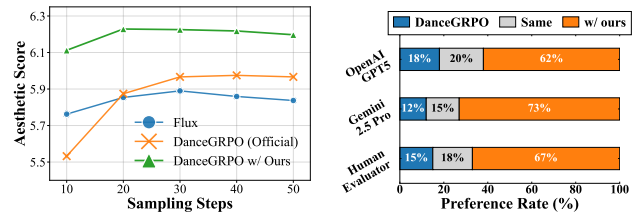


Figure 7. Results on sample steps. DanceGRPO adopt off-
Figure 8. Results on LLM eval-
uation and user study on human
preference.

from 665 to 541 (18.6% speedup, Fig. 6 (b)) and maintains a similar average out-of-domain score (2.52 vs. 2.49 in Tab. 4). Unlike best-of- N strategies that increase compute and often yield highly similar top/bottom- N samples, thus hindering late-stage optimization as diversity declines during RFT (Fig. 6 (b)), Intra-group DGS sustains diversity more efficiently with lower computational overhead.

Dynamic vs. Static Noise. To obtain high-quality positive samples, we use Gold Noise [82] for positive samples and Static Noise for negatives. Results are shown in Tab. 5.

More Results & Discussion. Additional results and analyses are provided in App. A, including qualitative evaluations, hyperparameter sensitivity, and further analyses.

7. Conclusion

In this work, we introduce ConsistentRFT, a general framework designed to mitigate visual hallucinations in RFT for flow models. Our framework proposes two key innovations: DGR to balance fine- and coarse-grained optimization, and CPGO to preserve the model’s predictive consistency. Extensive experiments show that ConsistentRFT achieves state-of-the-art performance, reducing visual hallucinations by up to 49% while improving out-of-domain generalization (+5.1% on FLUX1.dev).

Limitations. Although this work provides a preliminary
Table 5. Ablation on noise initialization strategies.

	SDXL	w/ Static	w/ Gold+Static		SDXL	w/ Static	w/ Gold+Static
Avg.	1.998	2.045	2.093	Uni.Rew.	3.425	3.472	3.536

investigation into visual hallucinations during post-training and proposes an initial mitigation strategy, we recognize that addressing this challenge requires not only a robust RFT method but also more powerful and scalable reward models [64]. We anticipate future developments of stronger open-source reward models by the community.

References

- [1] Ikhlas Abdel-Qader, Osama Abudayyeh, and Michael E. Kelly. Analysis of edge-detection techniques for crack identification in bridges. *Journal of computing in civil engineering*, 17(4):255–263, 2003. [23](#), [24](#)
- [2] Sumukh K Aithal, Pratyush Maini, Zachary Lipton, and J Zico Kolter. Understanding hallucinations in diffusion models through mode interpolation. *Advances in Neural Information Processing Systems*, 37:134614–134644, 2024. [2](#), [4](#), [6](#), [8](#)
- [3] Jinze Bai, Shuai Bai, Shusheng Yang, Shijie Wang, Sinan Tan, Peng Wang, Junyang Lin, Chang Zhou, and Jingren Zhou. Qwen-vl: A frontier large vision-language model with versatile abilities. *arXiv preprint arXiv:2308.12966*, 2023. [6](#), [25](#)
- [4] Lichen Bai, Shitong Shao, Zikai Zhou, Zipeng Qi, Zhiqiang Xu, Haoyi Xiong, and Zeke Xie. Zigzag diffusion sampling: Diffusion models can self-improve via self-reflection. *The Thirteenth International Conference on Learning Representations*, 2024. [5](#)
- [5] Raghav Bansal, Gaurav Raj, and Tanupriya Choudhury. Blur image detection using laplacian operator and open-cv. In *2016 International Conference System Modeling and Advancement in Research Trends (SMART)*, pages 63–67, 2016. [23](#)
- [6] Kevin Black, Michael Janner, Yilun Du, Ilya Kostrikov, and Sergey Levine. Training diffusion models with reinforcement learning. *arXiv preprint arXiv:2305.13301*, 2023. [2](#), [3](#), [6](#), [7](#), [8](#), [22](#)
- [7] Qi Cai, Jingwen Chen, Yang Chen, Yehao Li, Fuchen Long, Yingwei Pan, Zhaofan Qiu, Yiheng Zhang, Fengbin Gao, Peihan Xu, et al. Hidream-i1: A high-efficient image generative foundation model with sparse diffusion transformer. *arXiv preprint arXiv:2505.22705*, 2025. [2](#), [7](#)
- [8] Daniele Calandriello, Daniel Guo, Remi Munos, Mark Rowland, Yunhao Tang, Bernardo Avila Pires, Pierre Harvey Richemond, Charline Le Lan, Michal Valko, Tianqi Liu, et al. Human alignment of large language models through online preference optimisation. *arXiv preprint arXiv:2403.08635*, 2024. [3](#)
- [9] Changgu Chen, Libing Yang, Xiaoyan Yang, Lianggangxu Chen, Gaoqi He, Changbo Wang, and Yang Li. Find: Fine-tuning initial noise distribution with policy optimization for diffusion models. In *Proceedings of the 32nd ACM International Conference on Multimedia*, pages 6735–6744, 2024. [5](#)
- [10] Kevin Clark, Paul Vicol, Kevin Swersky, and David J Fleet. Directly fine-tuning diffusion models on differentiable rewards. *arXiv preprint arXiv:2309.17400*, 2023. [7](#), [8](#)
- [11] Fei Deng, Qifei Wang, Wei Wei, Tingbo Hou, and Matthias Grundmann. Prdp: Proximal reward difference prediction for large-scale reward finetuning of diffusion models. In *Proceedings of the IEEE/CVF Conference on Computer Vision and Pattern Recognition*, pages 7423–7433, 2024. [22](#)
- [12] Discus0434. Aesthetic-Predictor-v2-5: Siglip-based aesthetic score predictor. <https://github.com/discus0434/aesthetic-predictor-v2-5?tab=readme-ov-file>, 2024. Accessed: May 27, 2024. [6](#), [15](#)
- [13] Tim Dockhorn, Arash Vahdat, and Karsten Kreis. Score-based generative modeling with critically-damped langevin diffusion. *arXiv preprint arXiv:2112.07068*, 2021. [2](#)
- [14] Patrick Esser, Sumith Kulal, Andreas Blattmann, Rahim Entezari, Jonas Müller, Harry Saini, Yam Levi, Dominik Lorenz, Axel Sauer, Frederic Boesel, et al. Scaling rectified flow transformers for high-resolution image synthesis. *arXiv preprint arXiv:2403.03206*, 2024. [1](#), [2](#), [7](#)
- [15] Ying Fan, Olivia Watkins, Yuqing Du, Hao Liu, Moonkyung Ryu, Craig Boutilier, Pieter Abbeel, Mohammad Ghavamzadeh, Kangwook Lee, and Kimin Lee. Dpok: Reinforcement learning for fine-tuning text-to-image diffusion models. *Advances in Neural Information Processing Systems*, 36:79858–79885, 2023. [1](#), [2](#), [3](#), [22](#)
- [16] Shuai Fu, Jian Zhou, Qi Chen, Huang Jing, Huy Anh Nguyen, Xiaohan Liu, Zhixiong Zeng, Lin Ma, Quanshi Zhang, and Qi Wu. Counting hallucinations in diffusion models. *arXiv preprint arXiv:2510.13080*, 2025. [2](#), [4](#), [6](#)
- [17] Xiaolong Fu, Lichen Ma, Zipeng Guo, Gaojing Zhou, Chongxiao Wang, ShiPing Dong, Shizhe Zhou, Ximan Liu, Jingling Fu, Tan Lit Sin, et al. Dynamic-treerpo: Breaking the independent trajectory bottleneck with structured sampling. *arXiv preprint arXiv:2509.23352*, 2025. [2](#), [3](#), [23](#)
- [18] Dhruba Ghosh, Hannaneh Hajishirzi, and Ludwig Schmidt. Geneval: An object-focused framework for evaluating text-to-image alignment. *Advances in Neural Information Processing Systems*, 36:52132–52152, 2023. [6](#), [21](#), [22](#)
- [19] Daya Guo, Dejian Yang, Haowei Zhang, Junxiao Song, Peiyi Wang, Qihao Zhu, Runxin Xu, Ruoyu Zhang, Shirong Ma, Xiao Bi, et al. Deepseek-r1 incentivizes reasoning in llms through reinforcement learning. *Nature*, 645(8081):633–638, 2025. [3](#)
- [20] Xiaoxuan He, Siming Fu, Yuke Zhao, Wanli Li, Jian Yang, Dacheng Yin, Fengyun Rao, and Bo Zhang. Tempflow-grpo: When timing matters for grpo in flow models. *arXiv preprint arXiv:2508.04324*, 2025. [2](#), [3](#), [22](#)
- [21] Jonathan Ho, Ajay Jain, and Pieter Abbeel. Denoising diffusion probabilistic models. In *Advances in Neural Information Processing Systems*, pages 6840–6851, 2020. [3](#)
- [22] Kaiyi Huang, Chengqi Duan, Kaiyue Sun, Enze Xie, Zhen-guo Li, and Xihui Liu. T2i-compbench++: An enhanced and comprehensive benchmark for compositional text-to-image generation. *IEEE Transactions on Pattern Analysis and Machine Intelligence*, 2025. [6](#)
- [23] Lei Huang, Weijiang Yu, Weitao Ma, Weihong Zhong, Zhangyin Feng, Haotian Wang, Qianglong Chen, Weihua Peng, Xiaocheng Feng, Bing Qin, et al. A survey on hallucination in large language models: Principles, taxonomy,

challenges, and open questions. *ACM Transactions on Information Systems*, 43(2):1–55, 2025. 2

[24] Tero Karras, Miika Aittala, Timo Aila, and Samuli Laine. Elucidating the design space of diffusion-based generative models. *Advances in neural information processing systems*, 35:26565–26577, 2022. 2

[25] Jisoo Kim, Wooseok Seo, Junwan Kim, Seungho Park, Sooyeon Park, and Youngjae Yu. Vip: Iterative online preference distillation for efficient video diffusion models. In *Proceedings of the IEEE/CVF International Conference on Computer Vision*, pages 17235–17245, 2025. 3

[26] Seunghoi Kim, Chen Jin, Tom Diethe, Matteo Figini, Henry FJ Tregidgo, Asher Mollokandov, Philip Teare, and Daniel C Alexander. Tackling structural hallucination in image translation with local diffusion. In *European Conference on Computer Vision*, pages 87–103. Springer, 2024. 2, 4, 6

[27] Yuval Kirstain, Adam Polyak, Uriel Singer, Shahbuland Matiana, Joe Penna, and Omer Levy. Pick-a-pic: An open dataset of user preferences for text-to-image generation. *Advances in Neural Information Processing Systems*, 36: 36652–36663, 2023. 6, 15

[28] Black Forest Labs. Flux. <https://github.com/black-forest-labs/flux>, 2024. 2, 6, 7, 8, 15, 17

[29] Jack Lanchantin, Angelica Chen, Janice Lan, Xian Li, Swarnadeep Saha, Tianlu Wang, Jing Xu, Ping Yu, Weizhe Yuan, Jason E Weston, et al. Bridging offline and online reinforcement learning for llms. *arXiv preprint arXiv:2506.21495*, 2025. 3

[30] Junzhe Li, Yutao Cui, Tao Huang, Yingping Ma, Chun Fan, Miles Yang, and Zhao Zhong. Mixgrpo: Unlocking flow-based grpo efficiency with mixed ode-sde. *arXiv preprint arXiv:2507.21802*, 2025. 2, 3, 4, 6, 7, 8, 22

[31] Yuming Li, Yikai Wang, Yuying Zhu, Zhongyu Zhao, Ming Lu, Qi She, and Shanghang Zhang. Branchgrpo: Stable and efficient grpo with structured branching in diffusion models. *arXiv preprint arXiv:2509.06040*, 2025. 2, 3, 4, 23

[32] Zhimin Li, Jianwei Zhang, Qin Lin, Jiangfeng Xiong, Yanxin Long, Xinchi Deng, Yingfang Zhang, Xingchao Liu, Minbin Huang, Zedong Xiao, Dayou Chen, Jiajun He, Jia-hao Li, Wenyue Li, Chen Zhang, Rongwei Quan, Jianxiang Lu, Jiabin Huang, Xiaoxiao Yuan, Xiaoxiao Zheng, Yixuan Li, Jihong Zhang, Chao Zhang, Meng Chen, Jie Liu, Zheng Fang, Weiyang Wang, Jinbao Xue, Yangyu Tao, Jianchen Zhu, Kai Liu, Sihuan Lin, Yifu Sun, Yun Li, Dongdong Wang, Mingtao Chen, Zhichao Hu, Xiao Xiao, Yan Chen, Yuhong Liu, Wei Liu, Di Wang, Yong Yang, Jie Jiang, and Qinglin Lu. Hunyuan-dit: A powerful multi-resolution diffusion transformer with fine-grained chinese understanding, 2024. 1, 2, 7

[33] Yaron Lipman, Ricky TQ Chen, Heli Ben-Hamu, Maximilian Nickel, and Matt Le. Flow matching for generative modeling. *arXiv preprint arXiv:2210.02747*, 2022. 1, 2, 19

[34] Buhua Liu, Shitong Shao, Bao Li, Lichen Bai, Zhiqiang Xu, Haoyi Xiong, James Kwok, Sumi Helal, and Zeke Xie. Alignment of diffusion models: Fundamentals, challenges, and future. *arXiv preprint arXiv:2024.07253*, 2024. 1, 2, 22

[35] Jie Liu, Gongye Liu, Jiajun Liang, Yangguang Li, Jiaheng Liu, Xintao Wang, Pengfei Wan, Di Zhang, and Wanli Ouyang. Flow-grpo: Training flow matching models via online rl. *arXiv preprint arXiv:2505.05470*, 2025. 2, 3, 7, 15, 21, 22

[36] Lu Liu, Huiyu Duan, Qiang Hu, Liu Yang, Chunlei Cai, Tianxiao Ye, Huayu Liu, Xiaoyun Zhang, and Guangtao Zhai. F-bench: Rethinking human preference evaluation metrics for benchmarking face generation, customization, and restoration. In *Proceedings of the IEEE/CVF International Conference on Computer Vision*, pages 10982–10994, 2025. 6

[37] Xingchao Liu, Chengyue Gong, and Qiang Liu. Flow straight and fast: Learning to generate and transfer data with rectified flow. *arXiv preprint arXiv:2209.03003*, 2022. 1, 2

[38] Cheng Lu, Yuhao Zhou, Fan Bao, Jianfei Chen, Chongxuan Li, and Jun Zhu. Dpm-solver: A fast ode solver for diffusion probabilistic model sampling in around 10 steps. *Advances in neural information processing systems*, 35:5775–5787, 2022. 2

[39] Yuhang Ma, Xiaoshi Wu, Keqiang Sun, and Hongsheng Li. Hpsv3: Towards wide-spectrum human preference score. In *Proceedings of the IEEE/CVF International Conference on Computer Vision*, pages 15086–15095, 2025. 6

[40] Trevine Oorloff, Yaser Yacoob, and Abhinav Shrivastava. Mitigating hallucinations in diffusion models through adaptive attention modulation. *arXiv preprint arXiv:2502.16872*, 2025. 2, 4, 6

[41] Yuang Peng, Yuxin Cui, Haomiao Tang, Zekun Qi, Runpei Dong, Jing Bai, Chunrui Han, Zheng Ge, Xiangyu Zhang, and Shu-Tao Xia. Dreambench++: A human-aligned benchmark for personalized image generation. *arXiv preprint arXiv:2406.16855*, 2024. 6

[42] Dustin Podell, Zion English, Kyle Lacey, Andreas Blattmann, Tim Dockhorn, Jonas Müller, Joe Penna, and Robin Rombach. Sdxl: Improving latent diffusion models for high-resolution image synthesis. *arXiv preprint arXiv:2307.01952*, 2023. 2, 7

[43] Xinyu Pu, Hongsong Wang, Jie Gui, and Pan Zhou. Dragging with geometry: From pixels to geometry-guided image editing. *arXiv preprint arXiv:2509.25740*, 2025. 1

[44] Alec Radford, Jong Wook Kim, Chris Hallacy, Aditya Ramesh, Gabriel Goh, Sandhini Agarwal, Girish Sastry, Amanda Askell, Pamela Mishkin, Jack Clark, et al. Learning transferable visual models from natural language supervision. In *International conference on machine learning*, pages 8748–8763. PMLR, 2021. 6, 15, 16

[45] Meisam Rakhshanfar and Maria A. Amer. Estimation of gaussian, poissonian-gaussian, and processed visual noise and its level function. *IEEE Transactions on Image Processing*, 25(9):4172–4185, 2016. 24

[46] Jiayuan Sheng, Hanyang Zhao, Haoxian Chen, David D. Yao, and Wenpin Tang. Understanding sampler stochasticity in training diffusion models for rlhf. *arXiv preprint arXiv:2510.10767*, 2025. 3, 23

[47] Dong-Hyuk Shin, Rae-Hong Park, Seungjoon Yang, and Jae-Han Jung. Block-based noise estimation using adaptive gaussian filtering. *IEEE Transactions on Consumer Electronics*, 51(1):218–226, 2005. 24

[48] Jiaming Song, Chenlin Meng, and Stefano Ermon. Denoising diffusion implicit models. In *International Conference on Learning Representations*, 2021. 3

[49] Yang Song, Jascha Sohl-Dickstein, Diederik P Kingma, Abhishek Kumar, Stefano Ermon, and Ben Poole. Score-based generative modeling through stochastic differential equations. *arXiv preprint arXiv:2011.13456*, 2020. 2

[50] Yang Song, Prafulla Dhariwal, Mark Chen, and Ilya Sutskever. Consistency models. *arXiv preprint arXiv:2303.01469*, 2023. 6, 32

[51] Zihan Su, Xuerui Qiu, Hongbin Xu, Tangyu Jiang, Junhao Zhuang, Chun Yuan, Ming Li, Shengfeng He, and Fei Richard Yu. Safe-sora: Safe text-to-video generation via graphical watermarking. *arXiv preprint arXiv:2505.12667*, 2025. 2

[52] Zihan Su, Hongyang Wei, Kangrui Cen, Yong Wang, Guanhua Chen, Chun Yuan, and Xiangxiang Chu. Generation enhances understanding in unified multimodal models via multi-representation generation, 2026. 1

[53] Xiaofeng Tan, Hongsong Wang, Xin Geng, and Pan Zhou. Sopo: Text-to-motion generation using semi-online preference optimization. *arXiv preprint arXiv:2412.05095*, 2024. 2

[54] Kolors Team. Kolors: Effective training of diffusion model for photorealistic text-to-image synthesis. *arXiv preprint*, 2024. 2, 7

[55] Chengzhuo Tong, Ziyu Guo, Renrui Zhang, Wenyu Shan, Xinyu Wei, Zhenghao Xing, Hongsheng Li, and Pheng-Ann Heng. Delving into rl for image generation with cot: A study on dpo vs. grp. *arXiv preprint arXiv:2505.17017*, 2025. 22

[56] Bram Wallace, Meihua Dang, Rafael Rafailev, Linqi Zhou, Aaron Lou, Senthil Purushwalkam, Stefano Ermon, Caiming Xiong, Shafiq Joty, and Nikhil Naik. Diffusion model alignment using direct preference optimization. In *Proceedings of the IEEE/CVF Conference on Computer Vision and Pattern Recognition*, pages 8228–8238, 2024. 1, 2, 3, 6, 7, 22

[57] Feng Wang and Zihao Yu. Coefficients-preserving sampling for reinforcement learning with flow matching. *arXiv preprint arXiv:2509.05952*, 2025. 2, 3, 23

[58] Yibin Wang, Zhimin Li, Yuhang Zang, Yujie Zhou, Jiazi Bu, Chunyu Wang, Qinglin Lu, Cheng Jin, and Jiaqi Wang. Pref-grpo: Pairwise preference reward-based grp for stable text-to-image reinforcement learning. *arXiv preprint arXiv:2508.20751*, 2025. 2, 3, 7, 8, 22, 25

[59] Yibin Wang, Yuhang Zang, Hao Li, Cheng Jin, and Jiaqi Wang. Unified reward model for multimodal understanding and generation. *arXiv preprint arXiv:2503.05236*, 2025. 4, 6, 15

[60] Min Wei, Jingkai Zhou, Junyao Sun, and Xuesong Zhang. Adversarial score distillation: When score distillation meets gan. In *Proceedings of the IEEE/CVF Conference on Computer Vision and Pattern Recognition (CVPR)*, pages 8131–8141, 2024. 19

[61] Wanjiang Weng, Xiaofeng Tan, Junbo Wang, Guo-Sen Xie, Pan Zhou, and Hongsong Wang. Realign: Text-to-motion generation via step-aware reward-guided alignment. *arXiv preprint arXiv:2511.19217*, 2025. 2

[62] Mitchell Wortsman, Gabriel Ilharco, Jong Wook Kim, Mike Li, Simon Kornblith, Rebecca Roelofs, Raphael Gontijo Lopes, Hannaneh Hajishirzi, Ali Farhadi, Hongseok Namkoong, et al. Robust fine-tuning of zero-shot models. In *Proceedings of the IEEE/CVF conference on computer vision and pattern recognition*, pages 7959–7971, 2022. 7, 8

[63] Chenfei Wu, Jiahao Li, Jingren Zhou, Junyang Lin, Kaiyuan Gao, Kun Yan, Sheng-ming Yin, Shuai Bai, Xiao Xu, Yilei Chen, et al. Qwen-image technical report, 2025. 2, 7

[64] Jie Wu, Yu Gao, Zilyu Ye, Ming Li, Liang Li, Hanzhong Guo, Jie Liu, Zeyue Xue, Xiaoxia Hou, Wei Liu, Yan Zeng, and Weilin Huang. Rewarddnce: Reward scaling in visual generation, 2025. 9

[65] Xiaoshi Wu, Yiming Hao, Keqiang Sun, Yixiong Chen, Feng Zhu, Rui Zhao, and Hongsheng Li. Human preference score v2: A solid benchmark for evaluating human preferences of text-to-image synthesis. *arXiv preprint arXiv:2306.09341*, 2023. 2, 6, 15, 17

[66] Yihong Wu, Liheng Ma, Lei Ding, Muzhi Li, Xinyu Wang, Kejia Chen, Zhan Su, Zhanguang Zhang, Chenyang Huang, Yingxue Zhang, et al. It takes two: Your grp is secretly dpo. *arXiv preprint arXiv:2510.00977*, 2025. 22

[67] Xin Xie and Dong Gong. Dymo: Training-free diffusion model alignment with dynamic multi-objective scheduling. In *2025 IEEE/CVF Conference on Computer Vision and Pattern Recognition (CVPR)*, pages 13220–13230, 2025. 6

[68] Jiazheng Xu, Xiao Liu, Yuchen Wu, Yuxuan Tong, Qinkai Li, Ming Ding, Jie Tang, and Yuxiao Dong. Imageward: Learning and evaluating human preferences for text-to-image generation. *Advances in Neural Information Processing Systems*, 36:15903–15935, 2023. 4, 6, 15, 16, 17, 21

[69] Zeyue Xue, Jie Wu, Yu Gao, Fangyuan Kong, Lingting Zhu, Mengzhao Chen, Zhiheng Liu, Wei Liu, Qiushan Guo, Weilin Huang, et al. Dancegrpo: Unleashing grp on visual generation. *arXiv preprint arXiv:2505.07818*, 2025. 2, 3, 4, 6, 7, 8, 18, 21, 22

[70] GitHub Users XueZeyue. Discussion on dancegrpo issue 36. <https://github.com/XueZeyue/DanceGRPO/issues/36>, 2025. Accessed: 2025-07-18. 2

[71] GitHub Users XueZeyue. Discussion on dancegrpo issue 72. <https://github.com/XueZeyue/DanceGRPO/issues/72>, 2025. Accessed: 2025-09-16. 22

[72] Kai Yang, Jian Tao, Jiafei Lyu, Chunjiang Ge, Jiaxin Chen, Weihan Shen, Xiaolong Zhu, and Xiu Li. Using human feedback to fine-tune diffusion models without any reward model. In *Proceedings of the IEEE/CVF Conference on Computer Vision and Pattern Recognition*, pages 8941–8951, 2024. 1, 2, 3, 7, 8, 22

[73] Yang Ye, Tianyu He, Shuo Yang, and Jiang Bian. Reinforcement learning with inverse rewards for world model post-training. *arXiv preprint arXiv:2509.23958*, 2025. 3, 23

[74] Benjamin Yu, Jackie Liu, and Justin Cui. Smart-grpo: Smartly sampling noise for efficient rl of flow-matching models. *arXiv preprint arXiv:2510.02654*, 2025. 2, 3, 23

[75] Shihao Yuan, Yahui Liu, Yang Yue, Jingyuan Zhang, Wangmeng Zuo, Qi Wang, Fuzheng Zhang, and Guorui Zhou. Argro: Training autoregressive image generation models via

reinforcement learning. *arXiv preprint arXiv:2508.06924*, 2025. 3, 23

[76] Fan Zhang and Michael Gienger. Affordance-based robot manipulation with flow matching. *arXiv preprint arXiv:2409.01083*, 2024. 1

[77] Guohui Zhang, Hu Yu, Xiaoxiao Ma, JingHao Zhang, Yaning Pan, Mingde Yao, Jie Xiao, Linjiang Huang, and Feng Zhao. Group critical-token policy optimization for autoregressive image generation. *arXiv preprint arXiv:2509.22485*, 2025. 3, 23

[78] Yinan Zhang, Eric Tzeng, Yilun Du, and Dmitry Kislyuk. Large-scale reinforcement learning for diffusion models. In *European Conference on Computer Vision*, pages 1–17. Springer, 2024. 2

[79] Yue Zhang, Yafu Li, Leyang Cui, Deng Cai, Lemao Liu, Tingchen Fu, Xinting Huang, Enbo Zhao, Yu Zhang, Yulong Chen, et al. Siren’s song in the ai ocean: A survey on hallucination in large language models. *Computational Linguistics*, pages 1–46, 2025. 2

[80] Kaiwen Zheng, Huayu Chen, Haotian Ye, Haoxiang Wang, Qinsheng Zhang, Kai Jiang, Hang Su, Stefano Ermon, Jun Zhu, and Ming-Yu Liu. Diffusionnft: Online diffusion reinforcement with forward process. *arXiv preprint arXiv:2509.16117*, 2025. 3, 23

[81] Yujie Zhou, Pengyang Ling, Jiazi Bu, Yibin Wang, Yuhang Zang, Jiaqi Wang, Li Niu, and Guangtao Zhai. G2rpo: Granular grp for precise reward in flow models. *arXiv preprint arXiv:2510.01982*, 2025. 2, 3, 23

[82] Zikai Zhou, Shitong Shao, Lichen Bai, Shufei Zhang, Zhiqiang Xu, Bo Han, and Zeke Xie. Golden noise for diffusion models: A learning framework. In *Proceedings of the IEEE/CVF International Conference on Computer Vision (ICCV)*, pages 17688–17697, 2025. 5, 8

[83] Djemel Ziou and Salvatore Tabbone. Edge detection techniques-an overview. *Pattern Recognition and Image Analysis: Advances in Mathematical Theory and Applications*, 8(4):537–559, 1998. 24

ConsistentRFT: Reducing Visual Hallucinations in Flow-based Reinforcement Fine-Tuning

Supplementary Material



Figure S1. Visualization Results.

Contents of Supplementary Material

A. Additional Experiments Results	14
A.1. Additional Quantitative Results	14
A.2. Additional Experiments Settings	15
A.3. Comparison of Fine-, Coarse-, and Dynamic Optimization Strategies	15
A.4. Coarse Progress Perception Results	15
A.5. Comparison between Initial Noise and Progressive Noise	17
A.6. Parameter Selection Discussion	18
B. Additional Method Details & Discussion	19
B.1. Additional Preliminaries	19
B.2. Algorithm	20
B.3. Details about Clustering-based Selection & Fine-Grained Refinement	21
B.4. Coarse- and Fine-Grained Optimization	21
B.5. Discussion about ConsistentRFT for Online DPO, DDPO & GRPO	22
C. Additional Related Works	22
D. Visual Hallucination Evaluator	23
D.1. Low-Level Evaluation	23
D.2. High-Level Evaluation	25
D.3. Visual Hallucination Evaluator Results	27
E. Theoretical Justification	28
E.1. Proof of Corollary 1	28
E.2. Corollary for DDPO & DPO	30
E.3. Theoretical Justification for CPGO	32
F. Visualization	32

This supplementary document provides additional quantitative and qualitative results, implementation details, theoretical justifications, and visualizations for ConsistentRFT. It is organized as follows. Sec. A reports additional experimental results, including extended quantitative comparisons, parameter sensitivity studies, and experimental settings. Sec. B provides further method details and discussion of our dynamic-granularity rollout and consistency regularization. Sec. C reviews additional related work on reinforcement fine-tuning and GRPO-style methods. Sec. D introduces the proposed visual hallucination evaluator, including low-level metrics, high-level MLLM-based assessment, and evaluation prompts, while Sec. E presents theoretical justifications for our training objectives and the CPGO regularizer. Finally, Sec. F provides visualizations.

A. Additional Experiments Results

This section presents comprehensive additional experimental results, including quantitative analyses, parameter sensitivity studies, and detailed experimental settings that support the main findings in the paper.

A.1. Additional Quantitative Results

This section summarizes the quantitative findings and sensitivity analyses presented in the following subsections. Below we provide quantitative and qualitative results for key analyses discussed throughout this supplementary document. Sec. A.3 presents a qualitative comparison of fine-, coarse-, and dynamic optimization strategies, demonstrating how our approach balances detail refinement and semantic diversity (see Fig. S9). Sec. A.4 reports quantitative metrics for Coarse Progress Perception, including cosine similarity across intermediate steps and ranking correlation with ImageReward, as shown in Fig. S2 and Fig. S3. Sec. A.5 quantifies the distinct roles of initial noise and progressive noise in generating diverse samples, with results presented in Fig. S5. Finally, Sec. A.6 provides comprehensive parameter sensitivity analysis in Table S2, with detailed hyperparameter analysis illustrated in Fig. S6. All results are supplemented by qualitative visualizations including Fig. S10 and Fig. S11 in Sec. F.

A.2. Additional Experiments Settings

Datasets & Models. For online settings, we use prompts from the HPDv2 [65] datasets for training and testing, following the HPS-v2 benchmark configuration. Considering that the existing post-training methods typically require fewer than 10k data prompts, we reserve the last 400 prompts from the training set with 103.7k prompts for validation. We employ FLUX.1 DEV [28] as our text-to-image model, using PickScore [27] as the reward for FlowGRPO [35] and HPS-v2.1 [65] for the remaining methods. For offline settings, we generate 20k image pairs using FLUX due to the insufficient quality of the HPDv2 dataset, with sample pairs determined by HPS-v2.1 scores.

Metrics. Following prior work, we evaluate our method using multiple metrics focused on diverse aspects, including human preference evaluators (ImageReward [68], PickScore [27]), an aesthetic model (Aesthetic Predictor v2.5 [12]), a semantic metric (CLIP Score [44]), and a comprehensive reward model (Unified Reward [59]). Particularly, the reward model used for training (e.g., HPS-v2.1) serves as the *in-domain metric*, while others are treated as *out-of-domain metrics*. Here, we suggest paying more attention to the out-of-domain metrics, as they reflect the model’s generalizability.

We evaluate visual hallucinations across three key aspects: (i) detail over-optimization, (ii) semantic consistency, and (iii) sampling trajectory consistency. Over-optimization is assessed using our HV-Evaluator, which combines low-level metrics with MLLM-based evaluation. Semantic consistency is measured by CLIP and Unified Reward scores, and trajectory consistency is determined by the straightness of the latent trajectory. Detailed descriptions of these metrics can be found in Sec. D.

Implementation. All experiments are conducted on 8 GPUs. Unless otherwise specified, we follow the official hyperparameter settings of baseline methods (see Table S1). For DanceGRPO, we adopt the standard configuration with $\eta = 0.3$, timestep fraction = 0.6, and clip range = 10^{-4} . For MixGRPO, we employ a mixed reward strategy with $\eta = 0.7$, progressive sampling with overlap, and multi-reward aggregation via advantage weighting. To ensure fair comparison, DPO and DDPO are configured to align with DanceGRPO’s base settings. Notably, since DPO optimizes via preference pairs rather than groups, we increase its batch size to 16 to maintain equivalent sample counts per iteration. For LoRA-based fine-tuning experiments, we set the LoRA rank to 128 and the LoRA scaling factor (α) to 256. Our method introduces additional hyperparameters: the CPGO weight ω , the inter-group DGS period, the coarse-grained ratio, and the intermediate perception step t_s . These are selected via validation set performance. For baseline methods in comparative experiments, the KL divergence weight is set to 10^{-6} , and early stopping is triggered when the in-domain metric on the validation set begins to decline (evaluated every 20 iterations). Parameter analysis for ConsistentRFT is provided in Sec. A.6. During evaluation, we adopt the same inference configuration as DanceGRPO. For all pretrained models in Tab. 2, we likewise strictly follow their official inference settings.

Table S1. Hyperparameter configurations for DanceGRPO and MixGRPO. MixGRPO-specific parameters are marked with \dagger .

Hyperparameter	DanceGRPO	MixGRPO
Learning Rate	$1e-5$	$1e-5$
Batch Size	2	2
Grad Accum Steps	12	3
Num Generations	12	12
Sampling Steps	16	25
Resolution	720×720	720×720
SDE Noise Weight (η)	0.3	0.7
Timestep Fraction	0.6	0.6
Clip Range	$1e-4$	$1e-4$
Max Grad Norm	0.01	1.0
Weight Decay	$1e-4$	$1e-4$
Adv Clip Max	5.0	5.0
Shift	3	3
Sample Strategy \dagger	SDE	SDE-ODE
DPM Solver \dagger	—	Yes

A.3. Comparison of Fine-, Coarse-, and Dynamic Optimization Strategies

Figure S9 presents a qualitative comparison of optimization strategies with different granularities. Fine-grained optimization tends to focus on local details, which can lead to over-optimization artifacts such as excessive sharpening and detail accumulation. Coarse-grained optimization, by contrast, maintains greater semantic diversity but may sacrifice fine-grained detail refinement. Our dynamic-grained optimization strategy balances both objectives by adaptively mixing coarse- and fine-grained rollouts, achieving improved visual quality with fewer hallucination artifacts.

A.4. Coarse Progress Perception Results

Experimental Settings. To assess the accuracy of the coarse progressive perception results relative to full-trajectory denoising, we conduct two analyses. We first select 50 prompts from HPDv2 [65]. For each prompt, using FLUX.1 dev [28] as the base model, we generate 12 images with 16 inference steps, a guidance scale of 3.5, and a resolution of 720×720 . (1) For each of the 16 intermediate steps, we store both the noisy images and their noise-aware perceptions, and compute cosine sim-

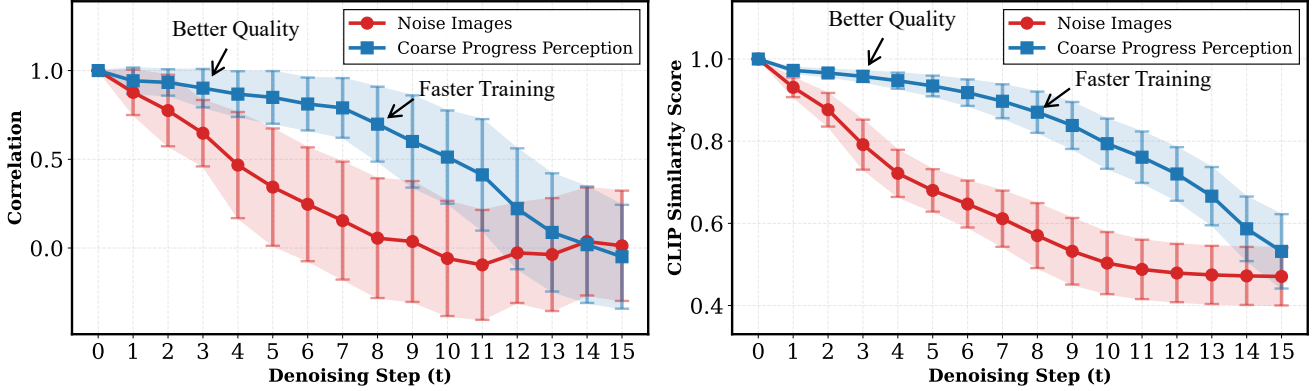


Figure S2. Coarse Progress Perception analysis. We compare the Coarse Progress Perception against full-trajectory denoising in terms of correlation between Coarse-Progress-Perception-derived rankings and ImageReward-based rankings (left) and cosine similarity across intermediate steps using CLIP ViT-L/14 features (right) over 12 images per prompt.

ilarity using CLIP ViT-L/14 features [44]. (2) We further investigate the correlation between the Coarse Progress Perception Results and rewards derived from full-trajectory denoising. Specifically, we adopt ImageReward [68] as the reward model to rank the 12 images generated for each prompt; we then rank the same set based on the Coarse Progress Perception Results and compare the two rankings to quantify their correlation. To ensure statistical significance and robustness, we conduct all experiments over 50 prompts with 50 independent repetitions each, and report the mean.

Results. We first present quantitative analyses. As shown in Fig. S2(a), we compare the similarity between noisy images at step t and their clean counterparts, together with the corresponding coarse progress perception. Fig. S2(b) reports the reward consistency between noisy images at step t and their noise-aware perceptions. The results indicate that our approach can

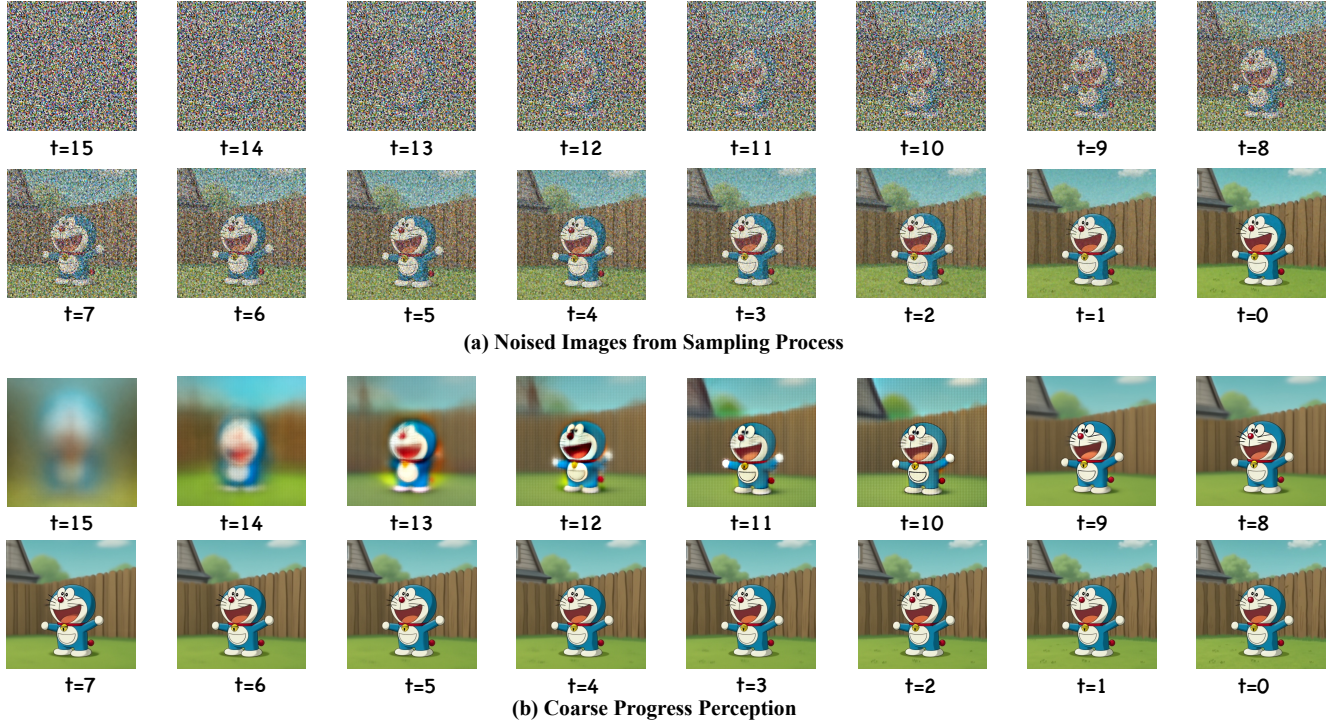


Figure S3. Visualization of noised images and their coarse perceptions. It can be observed that coarse progress perception facilitates earlier (smaller- t) recognition of image semantics and quality by the reward model.

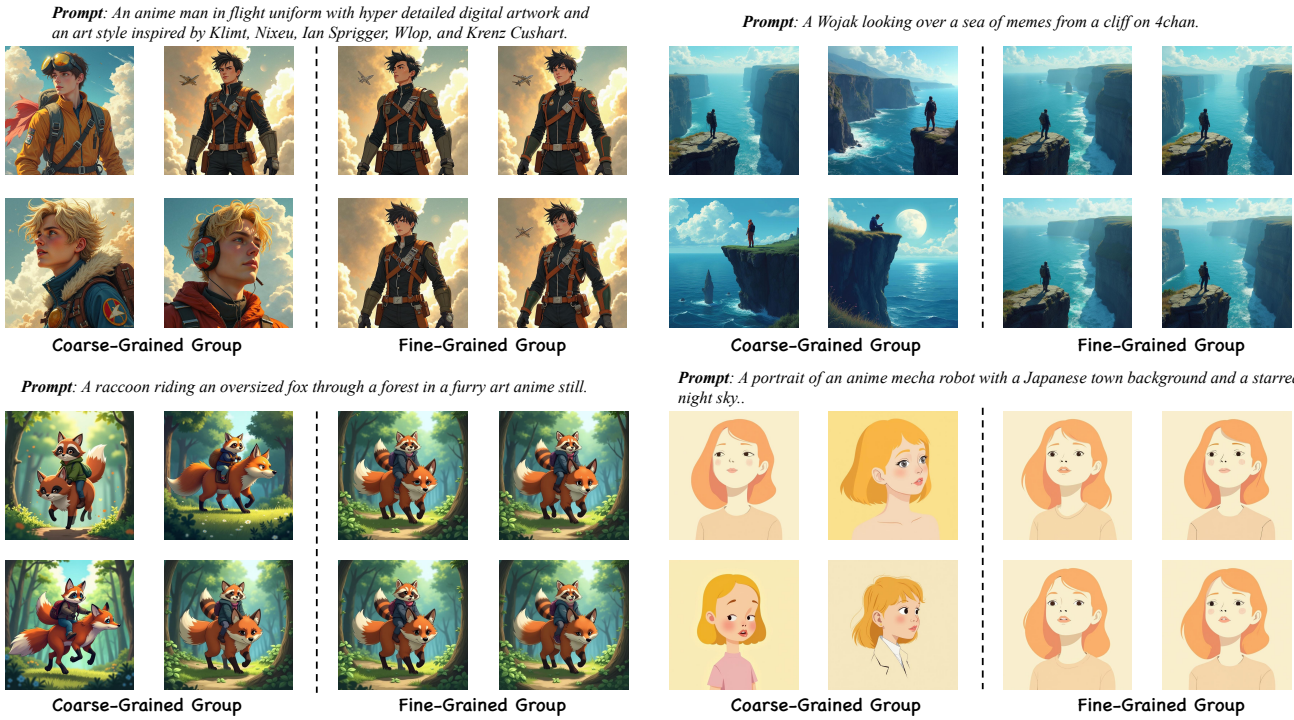


Figure S4. Visualization of coarse- and fine-grained groups. Coarse-grained groups exhibit greater variation in global semantics, whereas fine-grained groups show higher similarity in local details.

reliably anticipate image quality and semantics from intermediate trajectories. Based on this analysis, we recommend two thresholds for t_s : $t_s=12$ (for more accurate training; cf. the “ $t=4$ ” in the x -axis) and $t_s=8$ (for faster training; cf. the “ $t=8$ ” in the x -axis). We also provide qualitative examples in Fig. S3, which illustrate the same phenomena.

A.5. Comparison between Initial Noise and Progressive Noise

Experimental Settings. To compare the characteristics of initial noise and progressive (in-trajectory) noise, we quantitatively measure contrast and diversity for both coarse-grained and fine-grained groups. Concretely, we select 50 prompts from HPDv2 [65]. For each prompt, using FLUX.1 dev [28] as the base model, we generate 12 images with 16 inference steps, a guidance scale of 3.5, and a resolution of 720×720 . (1) For each group, we compute diversity as the variance in the CLIP feature space, that is, the trace of the covariance matrix. (2) In addition, we examine the dispersion of reward values within each group by reporting the standard deviation of ImageReward [68]. To ensure statistical significance and robustness, all experiments are conducted on 50 prompts with 50 independent repetitions per prompt, and we report the mean.

Results. As shown in Fig. S5, we compare coarse- and fine-grained groups with respect to diversity and contrast. Diversity

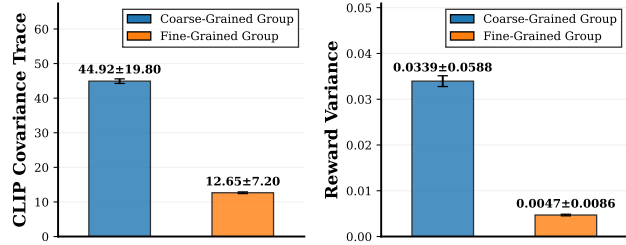


Figure S5. Comparison for fine-grained and coarse-grained groups in terms of (a) diversity and (b) contrast. The fine-grained group isolates randomness from progressive (in-trajectory) noise only, while the coarse-grained group includes randomness from both initial noise and progressive noise.

Table S2. Parameter Sensitivity Analysis.

Method	Period	Ratio	HPS-v2.1	ImageReward	PickScore	Aesthetic Pred. v2.5	CLIP Score	Unified Reward-S	Unified Reward	Avg.
Flux Dev (Base)	-	-	0.312	1.09	0.226	5.84	0.388	3.37	3.52	2.40
DanceGRPO [69]	-	-	0.353	1.16	0.226	5.90	0.361	3.30	3.38	2.39
ConsistentRFT	20	0.25	0.351	1.28	0.231	6.16	0.378	3.38	3.57	2.50
ConsistentRFT	50	0.25	0.346	1.29	0.229	6.13	0.387	3.43	3.60	2.51
ConsistentRFT	40	0.25	0.348	1.30	0.230	6.20	0.384	3.41	3.62	2.52
ConsistentRFT	40	0.75	0.342	1.25	0.228	6.04	0.389	3.46	3.55	2.49
ConsistentRFT	40	0.5	0.344	1.27	0.229	6.12	0.385	3.43	3.58	2.50
ConsistentRFT	40	0.25	0.348	1.30	0.230	6.20	0.384	3.41	3.62	2.52

is defined as the trace of the covariance matrix in the CLIP feature space, and contrast is measured by the standard deviation of ImageReward within each group. Quantitatively, the coarse-grained group exhibits markedly higher diversity and contrast than the fine-grained group. This pattern indicates that randomness attributable to initial noise, present only in the coarse-grained setting, primarily shapes global semantics, whereas progressive in-trajectory noise, shared by both settings, mainly affects local details. Consistent qualitative evidence is shown in Fig. S4, which further corroborates the distinct roles of initial and progressive noise in the generation process.

A.6. Parameter Selection Discussion

In this section, we discuss the key hyperparameters of our ConsistentRFT, including the period of the inter-group dynamic-grained rollout, the coarse-grained ratio, the coarse perception timestep in the intra-group dynamic-grained rollout, the weight of CPGO, and the threshold used to filter unreliable timesteps. All hyperparameters are determined either from validation experiments or heuristic studies (e.g., Fig. S2). Moreover, when applying our method to DPO and DDPO, we simply align their hyperparameter settings with those of DanceGRPO without additional tuning, highlighting the robustness and transferability of our hyperparameter choices. In practice, choosing appropriate hyperparameters is crucial; in what follows, we provide practical guidelines for selecting them.

Coarse Perception Timestep t_s . The coarse perception timestep t_s specifies the denoising step at which we perform Coarse Progress Perception, allowing an intermediate noisy sample to serve as a proxy for the final clean image. To determine a suitable value of t_s , we conduct an empirical study in which, for each candidate timestep, we (i) measure the similarity between noisy and clean samples and (ii) compute the correlation between Coarse Progress Perception and full-trajectory rewards (see Fig. S2). These analyses show that the reward signal becomes increasingly predictive as t_s moves towards later steps. Based on these results, we set $t_s=12$ as our default choice and additionally consider a faster variant with $t_s=8$, which provides a favorable trade-off between accuracy and efficiency. Therefore, for fine-tuning methods with a different number of

Prompt: a train on a track with a car nearby.



Base Model



$\omega = 10^{-5}$



$\omega = 10^{-6}$

Figure S6. Effect of the CPGO weight ω on optimization. A larger weight (e.g., 10^{-5}) can cause saturation, while moderate values (10^{-6} or less) strike a better balance between constraint strength and optimization flexibility.

sampling steps (i.e., other than 16), we recommend a simple visualization experiment similar to Fig. S2 to choose t_s , which only takes about 10 minutes for computation.

Weight of CPGO ω . The CPGO weight ω controls the strength of the consistency constraint that encourages the ODE-based prediction in CPGO to mimic the SDE sampling trajectory used by GRPO. Empirically, we observe that the GRPO loss is on the order of 10^{-7} , whereas the CPGO loss is typically around 10^{-4} . Since CPGO acts as a regularization term, we recommend searching ω in $\{10^{-5}, 10^{-6}, 10^{-7}\}$ so that the CPGO loss remains 2–4 orders of magnitude smaller than the GRPO loss. As illustrated in Fig. S6, setting $\omega = 10^{-5}$ can lead to saturation phenomena reminiscent of over-strong distillation effects in adversarial score distillation [60], while $\omega = 10^{-6}$ or smaller yields more desirable behavior, with smaller values gradually weakening the effect of the constraint. In practice, we therefore recommend choosing ω between 10^{-6} and 10^{-7} . In all our experiments, we uniformly fix $\omega = 10^{-6}$ for DPO, DDPO, and GRPO.

Period of Inter-Group DGR and Coarse-Grained Rollout Ratio. We analyze the sensitivity of the method to two key hyperparameters: the period controlling the switching frequency between coarse-grained and fine-grained optimization, and the ratio governing the proportion of coarse-grained rollouts. To balance the effectiveness of each optimization type, we recommend selecting the period from $\{20, 40, 50\}$ and the ratio from $\{0.25, 0.5, 0.75\}$. A more detailed discussion of how the coarse-grained ratio interacts with different types of reward functions is provided in Sec. B.4. The results in Table S2 align with the analysis presented in Section A.3. Both excessively small and large periods tend to diminish performance. Importantly, the method demonstrates robustness to these hyperparameter choices, with relatively stable results across different configurations.

B. Additional Method Details & Discussion

This section provides implementation details, training algorithms, clustering mechanisms, and unified comparisons across GRPO, DPO, and DDPO.

B.1. Additional Preliminaries

Flow matching [33] trains a time-dependent velocity field $v_\theta(\mathbf{x}_t, t)$ that transports a simple prior distribution to the data distribution via continuous-time dynamics. We summarize the training objective and inference procedure below.

Training Objective. The flow matching loss minimizes the discrepancy between the learned velocity field and a target conditional velocity along an interpolation path:

$$\mathcal{L}_{\text{FM}}(\theta) = \mathbb{E}_{t \sim \mathcal{U}(0,1), \mathbf{x}_0 \sim p_{\text{data}}, \mathbf{x}_1 \sim \mathcal{N}(\mathbf{0}, \sigma^2 \mathbf{I})} [\|v_\theta(\mathbf{x}_t, t) - u_t(\mathbf{x}_t \mid \mathbf{x}_0, \mathbf{x}_1)\|_2^2], \quad (\text{S1})$$

where the linear interpolation and target velocity are defined by

$$\mathbf{x}_t = (1 - t) \mathbf{x}_0 + t \mathbf{x}_1, \quad u_t(\mathbf{x}_t \mid \mathbf{x}_0, \mathbf{x}_1) = \mathbf{x}_1 - \mathbf{x}_0. \quad (\text{S2})$$

This formulation directly regresses the network output v_θ to the conditional flow velocity u_t , avoiding path simulation and enabling efficient training.

Inference via ODE. Image synthesis proceeds by solving the probability flow ODE using the learned velocity field:

$$\frac{d\mathbf{x}}{dt} = v_\theta(\mathbf{x}_t, t), \quad \mathbf{x}_1 \sim \mathcal{N}(\mathbf{0}, \sigma^2 \mathbf{I}), \quad (\text{S3})$$

which integrates backward from $t=1$ (noise distribution) to $t=0$ (real data distribution). A first-order Euler solver with T discrete steps $1 = t_0 > t_1 > \dots > t_T = 0$ yields

$$\mathbf{x}_{t_{n+1}} = \mathbf{x}_{t_n} + (t_{n+1} - t_n) v_\theta(\mathbf{x}_{t_n}, t_n). \quad (\text{S4})$$

The single-step ODE prediction function is

$$\pi_\theta^{\text{ODE}}(\mathbf{x}_t, t) := \mathbf{x}_t - t v_\theta(\mathbf{x}_t, t), \quad (\text{S5})$$

which recovers a clean estimate from an intermediate state using the learned velocity.

Algorithm 1 ConsistentRFT Training Algorithm

Require: Velocity field $v_\theta(\cdot, \cdot, \cdot)$, reward model $r(\cdot, \cdot)$, prompt dataset \mathcal{D}_c , group size K , intermediate step t_s , cluster size K_1

Ensure: Optimized velocity field v_θ

- 1: **for** iteration $m = 1, \dots, M$ **do**
- 2: Sample prompts $\mathcal{D}_b \sim \mathcal{D}_c$
- 3: **for** prompt $c \in \mathcal{D}_b$ **do**
- 4: ▷ **Exploration: Dynamic Granularity Rollout**
- 5: **if** *Fine-Grained Exploration* **then**
- 6: Initialize K Gaussian noises via $\{\mathbf{x}_T^k\}_{k=1}^K = \{\mathbf{x}_T^k \mid \mathbf{x}_T^k \stackrel{\text{i.i.d.}}{\sim} \mathcal{N}(\mathbf{0}, \mathbf{I})\}$
- 7: **else**
- 8: Initialize K Gaussian noises via $\{\mathbf{x}_T^k \mid \mathbf{x}_T^k \leftarrow (\mathbf{x}_T \sim \mathcal{N}(\mathbf{0}, \mathbf{I}))\}$
- 9: **end if**
- 10: **for** $k = 1, \dots, K$ **do**
- 11: Compute velocities: $\{\mathbf{v}_t^k\}_{t \in [t_s, T]} \leftarrow v_\theta(\mathbf{x}_t^k, t, c)$, $\{\mathbf{v}_t^{k, \text{old}}\}_{t \in [t_s, T]} \leftarrow v_{\theta_{\text{old}}}(\mathbf{x}_t^k, t, c)$
- 12: SDE-based sampling: $\mathbf{x}_{t_s}^k = \mathbf{x}_T^k - \int_{t_s}^T (\mathbf{v}_t^k - \frac{1}{2} \varepsilon_t^2 \nabla \log p_t(\mathbf{x}_t^k)) dt + \int_{t_s}^T \varepsilon_t d\mathbf{w}_t^k$
- 13: Coarse perception: $\hat{\mathbf{x}}_0^k = \mathbf{x}_{t_s}^k - t_s \mathbf{v}_{t_s}^k$
- 14: **end for**
- 15: ▷ **Clustering-based Selection**
- 16: Compute latents: $\mathbf{z}^k \leftarrow \text{Enc}(\hat{\mathbf{x}}_0^k)$ for $k = 1, \dots, K$
- 17: Perform k -means clustering: $\mathcal{C} \leftarrow \text{KMeans}(\{\mathbf{z}^k\}_{k=1}^K, K_1)$
- 18: Select representative samples: $\mathcal{G}_1 \leftarrow \text{Select}(\{\mathbf{x}_{t_s}^k\}_{k=1}^K, \mathcal{C})$
- 19: Get complementary set: $\mathcal{G}_2 \leftarrow \{\mathbf{x}_{t_s}^k\}_{k=1}^K \setminus \mathcal{G}_1$
- 20: ▷ **Fine-Grained Refinement**
- 21: **for** $\mathbf{x}_{t_s}^k \in \mathcal{G}_1$ **do**
- 22: Compute velocities: $\{\mathbf{v}_t^k\}_{t \in [0, t_s]} \leftarrow v_\theta(\mathbf{x}_t^k, t, c)$, $\{\mathbf{v}_t^{k, \text{old}}\}_{t \in [0, t_s]} \leftarrow v_{\theta_{\text{old}}}(\mathbf{x}_t^k, t, c)$
- 23: SDE-Based sampling: $\mathbf{x}_0^k = \mathbf{x}_{t_s}^k - \int_0^{t_s} (\mathbf{v}_t^k - \frac{1}{2} \varepsilon_t^2 \nabla \log p_t(\mathbf{x}_t^k)) dt + \int_0^{t_s} \varepsilon_t d\mathbf{w}_t^k$ (Eq. (S6))
- 24: **end for**
- 25: ▷ **Reward Computation**
- 26: **for** group $\mathcal{G}_i \in \{\mathcal{G}_1, \mathcal{G}_2\}$ **do**
- 27: Compute rewards: $\{r_k = r(\mathbf{x}_0^k, c)\}_{k \in \mathcal{G}_i}$
- 28: Normalize advantages: $A_k \leftarrow (r_k - \bar{r}_i)/\sigma_{r,i}$ for $k \in \mathcal{G}_i$
- 29: Compute $\mathcal{J}_{\text{GRPO}}(\theta, \mathcal{G}_i)$
- 30: **end for**
- 31: ▷ **Policy Optimization**
- 32: Compute GRPO loss: $\mathcal{J}_{\text{GRPO}}(\theta, \mathcal{G}) = \mathcal{J}_{\text{GRPO}}(\theta, \mathcal{G}_1) + \mathcal{J}_{\text{GRPO}}(\theta, \mathcal{G}_2)$
- 33: **for** $t \in \mathcal{T}_{\text{sub}} \subseteq \{1, \dots, T\}$ **do**
- 34: ▷ **Consistency Policy Gradient Optimization (CPGO)**
- 35: **if** $t \geq \tau$ **then**
- 36: Compute $\mathcal{L}_{\text{CPGO}}(\theta, \mathcal{G}) = -\mathbb{E}_k \left[\left\| \pi_\theta^{\text{ODE}}(\mathbf{x}_t^k, t) - \pi_{\theta_{\text{old}}}^{\text{ODE}}(\mathbf{x}_{t-1}^k, t-1) \right\|_2^2 \right]$ (using velocities from L. 11 and 22)
- 37: **end if**
- 38: ▷ **Update Policy**
- 39: Compute total loss: $\mathcal{J}_{\text{ConsistentRFT}}(\theta, \mathcal{G}) = \mathcal{J}_{\text{GRPO}}(\theta, \mathcal{G}) + \omega \cdot \mathcal{L}_{\text{CPGO}}(\theta, \mathcal{G})$
- 40: Update θ via gradient descent on $\mathcal{J}_{\text{ConsistentRFT}}(\theta, \mathcal{G})$
- 41: **end for**
- 42: **end for**
- 43: **end for**

B.2. Algorithm

Algorithm 1 outlines the training pipeline of ConsistentRFT in a single pass per iteration: for each prompt, we conduct a dynamic-granularity rollout that initializes K trajectories (fine- or coarse-grained) and computes velocities over the coarse window ($t \in [t_s, T]$) while performing SDE sampling to obtain intermediate states and their coarse ODE perceptions; we then embed and cluster these perceptions to select a representative subset \mathcal{G}_1 and its complement \mathcal{G}_2 , and continue SDE sampling for \mathcal{G}_1 from t_s to 0, recording fine-grained velocities ($t \in [0, t_s]$) to furnish full-trajectory information; finally, we compute rewards and normalize advantages separately for \mathcal{G}_1 and \mathcal{G}_2 , and optimize a total objective that aggregates

GRPO losses from both groups with a consistency term (CPGO). Notably, CPGO requires no additional data: it reuses the velocities collected in the preceding stages to enforce cross-step consistency between consecutive ODE predictions, yielding a consistency constraint without extra collection overhead.

B.3. Details about Clustering-based Selection & Fine-Grained Refinement

Coarse-Grained Perception. Here, we revisit the main text and restate our objective: to sample a representative group. Starting from Gaussian noise $\mathbf{x}_T \sim \mathcal{N}(\mathbf{0}, \mathbf{I})$, we first perform t_s sampling steps to obtain the noisy samples and their corresponding coarse noise-aware perceptions, as follows:

$$\begin{cases} \mathbf{x}_{t_s}^k = \mathbf{x}_T^k - \int_{t_s}^T \left(\mathbf{v}_t^k - \frac{1}{2} \varepsilon_t^2 \nabla \log p_t(\mathbf{x}_t^k) \right) dt + \int_{t_s}^T \varepsilon_t d\mathbf{w}_t^k, \\ \hat{\mathbf{x}}_0^k = \mathbf{x}_{t_s}^k - t_s \mathbf{v}_{t_s}^k. \end{cases} \quad (\text{S6})$$

where $\mathbf{v}_t^k = v_\theta(\mathbf{x}_t^k, t)$ denotes the model-predicted velocity, ε_t is the noise schedule, \mathbf{w}_t^k is a standard Brownian motion, and t_s is the intermediate perception step. The estimate $\hat{\mathbf{x}}_0^k$ corresponds to the single-step ODE prediction $\pi_\theta^{\text{ODE}}(\mathbf{x}_{t_s}^k, t_s)$.

Clustering-based Selection. By Eq. (S6), we construct the group $\mathcal{G} = \{\mathbf{x}_t^k \mid k \in [1 : K], t \in [t_{\text{stop}} : T]\}$, which aggregates noisy intermediate states together with their coarse noise-aware perceptions (see Fig. S9). We first embed all elements of \mathcal{G} into a latent space via the encoder of reward model, and subsequently perform k -means clustering in the latent space to obtain K_1 cluster centers, $\{\mathbf{c}_i\}_{i=1}^{K_1}$:

$$\mathcal{C} = \{\mathbf{c}_i\}_{i=1}^{K_1} = \text{KMeans}(\text{Enc}(\mathcal{G}), K_1), \quad (\text{S7})$$

where $\text{Enc}(\cdot)$ denotes the reward model's encoder.

We then select a representative subset \mathcal{G}_1 by choosing the K_1 samples nearest to the cluster centers, and define the complementary subset, as follow:

$$\mathcal{G}_1 = \{\mathbf{x}_t^i\}_{i=1}^{K_1} = \text{Select}(\mathcal{G}, \mathcal{C}), \quad \mathcal{G}_2 = \mathcal{G} - \mathcal{G}_1, \quad (\text{S8})$$

where $\text{Select}(\cdot, \cdot)$ chooses the K_1 samples nearest to the centers.

Coarse-Grained Perception. To enrich \mathcal{G}_1 with full-trajectory information, we continue SDE-based sampling for the selected samples from the intermediate step to $t=0$, thereby completing their denoising trajectories:

$$\begin{aligned} \mathbf{x}_0^k &= \mathbf{x}_{t_s}^k - \int_0^{t_s} \left(\mathbf{v}_t^k - \frac{1}{2} \varepsilon_t^2 \nabla \log p_t(\mathbf{x}_t^k) \right) dt + \int_0^{t_s} \varepsilon_t d\mathbf{w}_t^k, \\ \mathcal{G}_f &\leftarrow \{\mathbf{x}_t^k \mid k \in [1 : K], t \in [0 : t_{\text{stop}}]\} \\ \mathcal{G}_1 &\leftarrow \mathcal{G}_1 \cup \mathcal{G}_f. \end{aligned} \quad (\text{S9})$$

In contrast, \mathcal{G}_2 retains only coarse, intermediate-level states. These two subsets at different granularities are optimized separately in subsequent stages.

Dual-Granularities Optimization. Here, we have obtained two groups at different granularities, \mathcal{G}_1 and \mathcal{G}_2 , where \mathcal{G}_1 aggregates representative, fully denoised, detail-rich samples and \mathcal{G}_2 retains coarser, intermediate-level samples. We optimize them separately:

$$\mathcal{J}_{\text{GRPO}}(\theta, \mathcal{G}) = \mathcal{J}_{\text{GRPO}}(\theta, \mathcal{G}_1) + \mathcal{J}_{\text{GRPO}}(\theta, \mathcal{G}_2).$$

B.4. Coarse- and Fine-Grained Optimization

Existing post-training methods for rectified flow models differ in how they balance coarse- and fine-grained exploration. Besides the fine-grained rollout strategy adopted by DanceGRPO [69] and its variants (see Sec. 4), some methods such as FlowGRPO [35] perform coarser exploration. *This discrepancy is largely driven by the underlying task and reward design.* DanceGRPO primarily targets *continuous, model-based rewards* (e.g., ImageReward [68] or HPS), where even subtle changes in local details can be reflected in the reward signal, making fine-grained exploration effective. In contrast, FlowGRPO adopts a *coarse-grained exploration scheme* that mainly adjusts global scene composition and object layout, making it difficult to focus on specific local regions and often leading to blurrier (See Fig. S11) and detail under-optimization (See Fig. S9).

In Sec. 6, we report quantitative results on model-based reward tasks comparing coarse- and fine-grained optimization. Here, we provide an additional perspective on object-centric compositional evaluation using the GenEval benchmark [18]. As summarized in Tab. S3, incorporating Dynamic Granularity Rollout (DGR) into FlowGRPO yields consistent improvements

Table S3. Results on the GenEval benchmark [18]. ‘‘Obj.’’ denotes object and ‘‘Attr.’’ denotes attribute. We report the compositional alignment scores for FlowGRPO with and without Dynamic Granularity Rollout (DGR).

Model	Overall	Single Obj.	Two Obj.	Counting	Colors	Position	Attr. Binding
FlowGRPO [35]	0.95	1.00	0.99	0.95	0.92	0.99	0.86
FlowGRPO w/ DGR (Ours)	0.96	1.00	0.99	0.97	0.93	0.98	0.89

across several GenEval categories, especially counting and attribute binding, without sacrificing performance on single- or two-object cases.

Beyond pure coarse- or fine-grained rollouts, our experiments indicate that dynamically mixing these granularities further improves robustness: coarse-grained exploration encourages semantic diversity at the scene level, while fine-grained refinement sharpens local details. This synergy is particularly beneficial for challenging object-centric prompts (e.g., small objects such as spoons), where the model must simultaneously place and render objects accurately. Overall, our dynamic-granularity rollout enables RFT methods to achieve better performance on tasks with both continuous and discrete reward signals.

B.5. Discussion about ConsistentRFT for Online DPO, DDPO & GRPO

In App. B.1, we presented online DPO, GRPO, and DDPO from a unified perspective as schemes that follow a common exploration, comparison, and update pattern over model-generated samples. Here we elaborate on this connection and explain why ConsistentRFT can consistently improve all three methods in the online setting.

Shared exploration and comparison paradigm. In the exploration stage, these methods sample candidate trajectories or images from the current policy. A reward model then scores these samples, and the learning signal is constructed by comparing samples within a shared context. GRPO explicitly performs group-wise comparison: it normalizes rewards within a prompt-level group to obtain advantages and uses these advantages as weights when updating the policy, thereby encouraging samples with higher group-relative rewards. Online DPO, by contrast, forms positive and negative preference pairs and maximizes the probability gap between preferred and unpreferred samples. Similar insights on contrastive learning have also been made in recent studies [55, 66].

The original DDPO formulation aggregates samples at the global level [69, 71], rather than organizing them into prompt-level groups. While this paradigm is conceptually simple, it becomes difficult to optimize stably at scale, especially when the reward landscape is highly heterogeneous across prompts [11, 71]. Recent works have reported pronounced instability [11, 71]. Motivated by the design of DanceGRPO, we therefore adopt a prompt-level group-based formulation for DDPO, while retaining its objective. This modification brings DDPO structurally closer to GRPO and DPO, and substantially improves optimization stability in our experiments.

Why ConsistentRFT unifies improvements across DPO, GRPO, and DDPO. Given that all three algorithms rely on exploration over trajectories and comparative feedback within groups or pairs, they can all benefit from dynamic-granularity rollout. ConsistentRFT provides such a rollout mechanism: it adaptively mixes coarse-grained exploration with fine-grained refinement and augments the base objective with a consistency regularizer that aligns ODE-based predictions with SDE trajectories. As a result, ConsistentRFT serves as a unified plug-in that consistently improves DPO, GRPO, and DDPO in the online setting.

C. Additional Related Works

Reinforcement Fine-Tuning Methods. Early works in reinforcement fine-tuning for diffusion models include DDPO [6], which adapts policy gradient methods from reinforcement learning to fine-tune text-to-image models. DPOK [15] extends this approach with improved reward modeling. Direct Preference Optimization (DPO) [56] simplifies the process by eliminating the need for explicit reward models, instead learning directly from preference pairs. D3PO [72] further refines this by incorporating human feedback without requiring a separate reward model. These methods have demonstrated significant improvements in aligning generated images with human preferences and complex semantic objectives [34].

Concurrent GRPO-Style Works. Building upon DanceGRPO [69] and Flow-GRPO [35], several concurrent works have explored orthogonal improvements to flow-based reinforcement fine-tuning. MixGRPO [30] combines ODE and SDE sampling strategies to unlock efficiency in flow-based GRPO, achieving better sample efficiency while maintaining generation quality by mixing deterministic and stochastic rollouts. Pref-GRPO [58] incorporates pairwise preference rewards to enable more stable text-to-image reinforcement learning, addressing the challenge of learning from relative preferences rather than absolute reward scores. TempFlow-GRPO [20] introduces temporal scheduling mechanisms that dynamically adjust

the optimization focus across different timesteps, recognizing that different stages of the generation process may require different optimization strategies. BranchGRPO [31] proposes structured branching in diffusion models to stabilize training dynamics and improve exploration efficiency during the rollout phase. Smart-GRPO [74] focuses on intelligent noise sampling strategies, smartly sampling noise to achieve more efficient reinforcement learning of flow-matching models. Wang et al. [57] introduce coefficients-preserving sampling methods to preserve important flow coefficients during the sampling process, maintaining the mathematical properties of the flow model. Dynamic-TreeRPO [17] breaks the independent trajectory bottleneck by introducing structured sampling with dynamic tree structures, enabling more flexible trajectory exploration. G2RPO [81] investigates granular GRPO for precise reward optimization in flow models, focusing on fine-grained reward signals at different generation stages. Sheng et al. [46] provide theoretical analysis on understanding sampler stochasticity in training diffusion models for RLHF, offering insights into the role of noise in the reinforcement learning process. DiffusionNFT [80] proposes online diffusion reinforcement with forward process, introducing a novel perspective on leveraging the forward diffusion process for more effective training. Beyond flow-based models, AR-GRPO [75] extends GRPO to autoregressive image generation models, demonstrating the versatility of group-based policy optimization across different generative paradigms. Similarly, Zhang et al. [77] introduce group critical-token policy optimization specifically designed for autoregressive image generation, focusing on identifying and optimizing critical tokens in the generation sequence. Ye et al. [73] explore reinforcement learning with inverse rewards for world model post-training, addressing the challenge of aligning video generation models with desired dynamics.

D. Visual Hallucination Evaluator

In this section, we describe the visual hallucination evaluator used to evaluate the performance of our method.

D.1. Low-Level Evaluation

We first describe the low-level image-space and latent-space metrics used by our visual hallucination evaluator to quantify detail over-optimization, artifacts, and noise level.

D.1.1. Laplacian Variance

Let $I : \Omega \rightarrow \mathbb{R}$ denote a grayscale image defined on domain $\Omega \subset \mathbb{Z}^2$. The Laplacian Variance [5] is defined as the variance of the discrete Laplacian operator applied to I :

$$\mathcal{S}(I) = \text{Var}(\nabla^2 I), \quad (\text{S10})$$

where the discrete Laplacian is given by

$$\nabla^2 I(x, y) = I(x+1, y) + I(x-1, y) + I(x, y+1) + I(x, y-1) - 4I(x, y), \quad (\text{S11})$$

and the variance is computed as

$$\text{Var}(\nabla^2 I) = \frac{1}{|\Omega|} \sum_{(x,y) \in \Omega} (\nabla^2 I(x, y) - \mu)^2, \quad (\text{S12})$$

where $\mu = \frac{1}{|\Omega|} \sum_{(x,y) \in \Omega} \nabla^2 I(x, y)$ is the mean of the Laplacian response.

The Laplacian operator [5] is a second-order differential operator that isolates high-frequency components of the image. In a sharp image, edges exhibit rapid intensity transitions, producing large-magnitude Laplacian responses with high variance. In contrast, blurred images exhibit smooth transitions with attenuated Laplacian responses and lower variance. This metric quantifies the degree of edge definition and is invariant to global intensity shifts.

D.1.2. High-Frequency Energy

Let $I : \Omega \rightarrow \mathbb{R}$ denote a grayscale image. The high-frequency energy [1] is defined as the mean absolute response of a high-pass filter applied to I :

$$\mathcal{E}_{\text{hf}}(I) = \frac{1}{|\Omega|} \sum_{(x,y) \in \Omega} |H(x, y)|, \quad (\text{S13})$$

where

$$H(x, y) = (I * K_{\text{hp}})(x, y) = \sum_{u,v} I(x-u, y-v) \cdot K_{\text{hp}}(u, v) \quad (\text{S14})$$

is the high-pass filtered image obtained via convolution, and the high-pass filter kernel K_{hp} is defined as

$$K_{\text{hp}} = \begin{bmatrix} -1 & -1 & -1 \\ -1 & 8 & -1 \\ -1 & -1 & -1 \end{bmatrix}. \quad (\text{S15})$$

High-frequency components represent rapid spatial variations in image intensity. The magnitude of high-frequency energy serves as an indicator of image complexity, texture richness, and potential artifacts. In the context of image enhancement, excessive high-pass filtering amplifies both legitimate details and noise, producing characteristic artifacts. The mean absolute response quantifies the overall magnitude of these high-frequency components.

D.1.3. Edge Metric

Let $I : \Omega \rightarrow \mathbb{R}$ denote a grayscale image. The edge metric quantifies ringing artifacts by measuring intensity variation in edge neighborhoods [1, 83].

Edge Detection. Edges are detected using the Canny edge detector:

$$E(x, y) = \text{Canny}(I; \tau_1, \tau_2), \quad (\text{S16})$$

where τ_1 and τ_2 are the lower and upper gradient magnitude thresholds, respectively. The Canny detector produces a binary edge map $E : \Omega \rightarrow \{0, 1\}$.

Morphological Dilation. The edge map is dilated to capture the edge neighborhood:

$$E_{\text{dil}}(x, y) = (E \oplus B)(x, y) = \max_{(u, v) \in B} E(x - u, y - v), \quad (\text{S17})$$

where \oplus denotes morphological dilation and B is a 3×3 structuring element. Dilation is applied iteratively $n = 2$ times to expand the edge region.

Artifact Quantification. The edge artifact metric is defined as the standard deviation of pixel intensities within the dilated edge region:

$$\mathcal{A}_{\text{edge}}(I) = \sqrt{\frac{1}{|M|} \sum_{(x, y) \in M} (I(x, y) - \bar{I}_M)^2}, \quad (\text{S18})$$

where $M = \{(x, y) \in \Omega : E_{\text{dil}}(x, y) > 0\}$ is the set of pixels in the dilated edge region, and $\bar{I}_M = \frac{1}{|M|} \sum_{(x, y) \in M} I(x, y)$ is the mean intensity in M .

Over-sharpening produces characteristic ringing artifacts at edges, manifesting as bright and dark halos adjacent to edge transitions (Gibbs phenomenon). These artifacts are characterized by abnormally high intensity variation in edge neighborhoods. By restricting the standard deviation computation to edge regions, this metric isolates the contribution of ringing artifacts while minimizing contamination from natural texture variation. The metric is grounded in the theory of edge-preserving filtering and artifact characterization.

D.1.4. Noise Estimation

Let $I : \Omega \rightarrow \mathbb{R}$ denote a grayscale image. The noise level is estimated from smooth (low-texture) regions where pixel variations are primarily attributable to noise [45, 47].

Local Texture Characterization. We first compute the local standard deviation at each pixel to characterize local texture:

$$\sigma_{\text{local}}(x, y) = \sqrt{\frac{1}{K^2} \sum_{(u, v) \in W(x, y)} (I(u, v) - \bar{I}_W)^2}, \quad (\text{S19})$$

where $W(x, y)$ is a square window of size $K \times K$ centered at (x, y) , and \bar{I}_W is the local mean within the window.

Smooth Region Identification. Smooth regions are identified as those with local standard deviation below the 30th percentile:

$$M_{\text{smooth}} = \{(x, y) \in \Omega : \sigma_{\text{local}}(x, y) < P_{30}(\sigma_{\text{local}})\}, \quad (\text{S20})$$

where P_{30} denotes the 30th percentile of the local standard deviation distribution.

Noise Map Computation. The noise map is computed as the absolute difference between the original image and a Gaussian-smoothed version:

$$N_{\text{map}}(x, y) = |I(x, y) - G_\sigma(I)(x, y)|, \quad (\text{S21})$$

where G_σ is a Gaussian low-pass filter with standard deviation $\sigma = 1.0$ and kernel size 5×5 .

Noise Level Estimation. The noise level is estimated as the mean of the noise map restricted to smooth regions:

$$\mathcal{L}_{\text{noise}}(I) = \frac{1}{|M_{\text{smooth}}|} \sum_{(x, y) \in M_{\text{smooth}}} N_{\text{map}}(x, y). \quad (\text{S22})$$

This metric quantifies the noise level by averaging noise map values over regions with minimal texture, providing a robust estimate of additive noise.

In smooth image regions with minimal texture, the difference between the original image and a slightly smoothed version approximates the noise component, as texture is attenuated by the smoothing operation while noise remains largely unchanged. By restricting this estimation to regions identified as smooth via local standard deviation, the metric avoids contamination from texture and edge structures. This approach is grounded in the principle that noise is signal-independent and spatially uncorrelated, while texture exhibits spatial correlation and concentrates in high-variance regions.

D.1.5. Latent Consistency

Flow matching models learn to transform noise into data by modeling a continuous-time ordinary differential equation (ODE). The latent consistency metric quantifies the deviation of the learned flow from the ideal linear interpolation path, providing a measure of trajectory stability and model fidelity.

Reverse Process. Given a flow matching model parameterized by velocity field $\mathbf{v}_\theta : \mathbb{R}^d \times [0, 1] \rightarrow \mathbb{R}^d$, the reverse sampling process follows the ODE

$$\begin{cases} \frac{d\mathbf{x}_t}{dt} = \mathbf{v}_\theta(\mathbf{x}_t, t), \\ \mathbf{x}_t = \mathbf{x}_1 - \int_1^t \mathbf{v}_\theta(\mathbf{x}_s, s) \, ds, \end{cases} \quad (\text{S23})$$

where $\mathbf{x}_t \in \mathbb{R}^d$ denotes the latent representation at time $t \in [0, 1]$, with $\mathbf{x}_1 \sim \mathcal{N}(\mathbf{0}, \mathbf{I})$ representing the initial noise and \mathbf{x}_0 the generated clean latent. The integral is typically approximated using numerical ODE solvers such as Euler or Runge–Kutta methods with T discrete timesteps.

Ideal Flow Trajectory. In the theoretical framework of flow matching, the optimal transport path between noise distribution $p_1 = \mathcal{N}(\mathbf{0}, \mathbf{I})$ and data distribution p_0 follows a linear interpolation. Given a clean latent \mathbf{x}_0 obtained via (S23) and initial noise $\mathbf{x}_1 \sim \mathcal{N}(\mathbf{0}, \mathbf{I})$, the ideal noised latent at time t is

$$\mathbf{x}_t^{\text{ideal}} = (1 - t) \cdot \mathbf{x}_0 + t \cdot \mathbf{x}_1, \quad t \in [0, 1]. \quad (\text{S24})$$

This represents the straight-line geodesic in latent space connecting the data point \mathbf{x}_0 to its corresponding noise sample \mathbf{x}_1 , which minimizes the transport cost under the L^2 metric.

Latent Consistency Metric. The latent consistency metric quantifies the deviation between the actual trajectory $\{\mathbf{x}_t\}_{t=0}^1$ produced by the learned model and the ideal linear path $\{\mathbf{x}_t^{\text{ideal}}\}_{t=0}^1$:

$$\text{Latent Consistency}(\mathbf{v}_\theta) = \frac{1}{\dim(\mathbf{x}_0)} \mathbb{E}_{t \sim [0, 1]} \|\mathbf{x}_t - \mathbf{x}_t^{\text{ideal}}\|_2^2, \quad (\text{S25})$$

where $\{t_i\}_{i=1}^T$ are uniformly spaced timesteps in $[0, 1]$, and \mathbf{x}_{t_i} is computed via (S23).

This metric serves as a diagnostic tool for assessing model quality: *Low consistency*: indicates that the learned flow deviates significantly from the optimal transport path, which suggests potential issues such as mode collapse, training instability, or over-optimization artifacts. *High consistency*: suggests that the model closely follows the theoretical optimal path and indicates stable training and faithful representation of the data distribution.

D.2. High-Level Evaluation

Similar to PredGRPO [58], we complement the low-level metrics with a high-level evaluation based on a pre-trained multi-modal large language model (MLLM), instantiated as Qwen-VL-72B [3]. To enable the model to understand the evaluation task, we adopt an in-context learning setup: the prompt includes an “Example Comparison” section that provides a reference pair illustrating different levels of over-optimization. The corresponding visual examples are shown in Fig. S7.

Prompt: A raccoon riding an oversized fox through a forest in a furry art anime still.



Example 1



Example 2



Example 3

Figure S7. Reference examples used in the VH-Evaluator prompt. The examples illustrate (i) accumulation of irrelevant details versus moderate detailing (Example 1 v.s. Example 2) and (ii) over-sharpened details versus natural sharpening (Example 1 v.s. Example 3), corresponding to the “Example Comparison” section in the prompt.

Evaluation Prompts

You are a professional image quality assessment expert specializing in evaluating over-optimization hallucination phenomena in images described by “<prompt>”.

(Author’s Note: In text-to-image generation, evaluation is naturally conditioned on prompts, but in other domains (e.g., image editing) such prompts may not exist or be well defined. Thus, <prompt> is optional.)

Over-Optimization Hallucination Definition

Over-optimization hallucination includes the following types:

1. Grid Pattern Artifacts

- Regular grid textures, repetitive patterns, and other artifacts appear
- Usually caused by the internal structure of generative models

2. Texture Over-Enhancement

- Over-enhanced texture details that make the image look unnatural
- Surfaces appear overly rough or overly smooth

Evaluation Task

Please evaluate the over-optimization hallucination phenomena in the following image:

Image to Evaluate: The image below

Scoring Criteria

- **Over-optimization Level:** 0–5 points, 0 means no problem at all, 5 means extremely severe
 - detail_sharpness_score: Detail sharpening level (edge harshness, unnatural sharpening, high-frequency noise)
 - irrelevant_details_score: Irrelevant details level (extra details unrelated to prompt, over-decoration, information overload)
 - grid_pattern_score: Grid texture level (extra grid behind the generated image)
- **Overall Hallucination Level:** Average of the above three items
- **Confidence:** 0–1, indicating your certainty about the scoring

Key Evaluation Points

1. Detail Inspection:

- Are there unnecessary detail accumulations?
- Are edges over-sharpened?

- Are there elements unrelated to the original intent?

2. **Naturalness Assessment:** Does the image look natural overall, or does it appear ‘‘over-processed’’?
3. **Artifact Detection:**
 - Look for grid patterns or repetitive textures
 - Check for over-enhanced or unnatural details
 - Identify any signs of over-optimization

Reference Examples

The following are three reference examples showing different types of over-optimization hallucination:

Example Comparison 1: Irrelevant Details Accumulation vs Moderate Details

- **Example 1 (Over-optimized):** Added a large number of irrelevant detail elements, generated excessive decorative content, appearing chaotic and information-overloaded
- **Example 2 (Moderately optimized):** Maintained moderate details without over-decoration, information is clear and well-organized
- **Key Difference:** Example 1’s irrelevant_details_score should be significantly higher than Example 2’s

Example Comparison 2: Over-Sharpended Details vs Natural Sharpening

- **Example 1 (Over-optimized):** Edges are over-sharpened, appearing harsh and unnatural, with obvious high-frequency noise and ‘‘over-refined’’ feeling
- **Example 3 (Moderately optimized):** Edge sharpening is moderate, maintaining naturalness, details are clear but not harsh
- **Key Difference:** Example 1’s detail_sharpness_score should be significantly higher than Example 3’s

Evaluation Guidance

When evaluating, please refer to these examples:

- When you see **large amounts of irrelevant details** similar to Example 1, increase irrelevant_details_score
- When you see **over-sharpened edges** similar to Example 1, increase detail_sharpness_score
- Example 2 and Example 3 represent more reasonable optimization levels and should receive lower hallucination scores

Return Format (Must be valid JSON)

```
{
  "image": {
    "has_over_optimization": true/false,
    "over_optimization_level": 0-5,
    "detail_sharpness_score": 0-5,
    "irrelevant_details_score": 0-5,
    "grid_pattern_score": 0-5,
    "overall_hallucination_score": 0-5,
    "confidence": 0-1,
    "detailed_analysis": "Detailed analysis description"
  }
}
```

Please carefully analyze the image and return the evaluation results in the above JSON format.

D.3. Visual Hallucination Evaluator Results

Fig. S8 displays qualitative evaluation results from the VH-Evaluator, showcasing images at varying degrees of over-optimization hallucination. The results illustrate how the MLLM-based evaluator successfully identifies and differentiates between different hallucination severity levels, from minor over-optimization artifacts to severe detail accumulation and sharpening artifacts.



```
{
  "image": {
    "has_over_optimization": true,
    "over_optimization_level": 2.23,
    "detail_sharpness_score": 3.2,
    "irrelevant_details_score": 3.5,
    "grid_pattern_score": 0.0,
    "overall_hallucination_score": 2.23,
    "confidence": 0.9,
    "detailed_analysis": "This image also demonstrates over-optimization. Texture is over-enhanced (3.2); details on the uniform's badges, embroidery, and sash are hyper-sharpened, creating an unnatural 'ultra-HD' texture that contrasts with the character's relatively smooth skin. There are too many irrelevant details (3.5); the uniform is covered in complex medals and decorations, and the background is extremely ornate, making the overall scene feel crowded and excessively decorated beyond what is necessary. No grid pattern artifacts were found (0.0)."
  }
}
```



```
{
  "image": {
    "has_over_optimization": true,
    "over_optimization_level": 2.00,
    "detail_sharpness_score": 3.0,
    "irrelevant_details_score": 3.0,
    "grid_pattern_score": 0.0,
    "overall_hallucination_score": 2.00,
    "confidence": 0.9,
    "detailed_analysis": "The image exhibits significant over-optimization issues. Detail sharpness is excessive (3.0), particularly noticeable in the edges of the character's hair, the metallic decorations on the uniform, and the intricate patterns in the background, which appear overly sharp and lack a natural feel. Additionally, the image contains numerous details loosely related to the core subject (3.0), such as the cluttered mirrors, frames, and various ornaments in the background, leading to information overload and excessive decoration. No grid pattern artifacts are present (0.0)."
  }
}
```



```
{
  "image": {
    "has_over_optimization": false,
    "over_optimization_level": 1.5,
    "detail_sharpness_score": 1.5,
    "irrelevant_details_score": 1.0,
    "grid_pattern_score": 0.0,
    "overall_hallucination_score": 0.83,
    "confidence": 0.95,
    "detailed_analysis": "The anime style of this image results in relatively minor over-optimization issues. The level of detail sharpening is low (1.5); while the lines of the hair and clothing are clear, this is consistent with the art style and does not create unnatural artifacts. The addition of irrelevant details is also restrained (1.0); the few decorations on the jacket and the airplanes in the background are consistent with the 'pilot' theme and do not cause information overload. The overall image appears coordinated, and no grid pattern artifacts are present (0.0)."
  }
}
```



Figure S8. Qualitative results from the VH-Evaluator demonstrating detection of over-optimization hallucinations at varying levels.

E. Theoretical Justification

In this section, we provide the corollaries for existing RFT methods, including GRPO, DPO, and DDPO, and theoretical justification for our CPGO.

E.1. Proof of Corollary 1

Corollary (Reinterpretation of GRPO). Given a flow model θ , a reward model $r(\mathbf{x}, c)$, and trajectories sampled via SDE in Eq. (1), the gradient of the GRPO satisfies

$$\nabla_{\theta} \mathcal{J}_{\text{GRPO}} = \begin{cases} 0, & \text{if } (u_1 \wedge v_1) \vee (u_2 \wedge \neg v_1), \\ \mathbb{E} \left[-\omega(t) \cdot \mathcal{A}^k \cdot \nabla_{\theta} \|\mu_{\theta}(\mathbf{x}_t, t, \mathbf{c}) - \mathbf{x}_{t-1}\|_2^2 \right], & \text{else.} \end{cases}$$

where $\mu_\theta(\cdot)$ denotes the mean value of predicted distribution of $p_\theta(\mathbf{x}_t \mid \mathbf{x}_{t-1})$, $\mathbb{I}(\cdot)$ is the indicator function, and conditions u_1 and u_2 are defined as follows:

$$u_1 \leftarrow \mathbb{I}(\rho_{t,i} \leq 1 - \epsilon), \quad u_2 \leftarrow \mathbb{I}(\rho_{t,i} \geq 1 + \epsilon), \quad v_1 \leftarrow \mathbb{I}(\mathcal{A}^k < 0).$$

Proof of Corollary 1. We prove that the clipped GRPO gradient either vanishes under clipping or coincides with the gradient of a weighted squared-error objective for the flow model's mean prediction. The standard clipped policy gradient objective for GRPO is:

$$\mathcal{J}_{\text{GRPO}}(\theta) = \mathbb{E}_{\mathbf{c} \sim \mathcal{D}_c, \mathbf{x}_t^i \sim \pi_{\theta_{\text{old}}}(\cdot \mid \mathbf{c})} [\min(\rho_{t,i} A_i, \text{clip}(\rho_{t,i}, 1 - \epsilon, 1 + \epsilon) A_i)] \quad (\text{S26})$$

where $\rho_{t,i} = \frac{p_\theta(\mathbf{x}_t^i \mid \mathbf{x}_{t-1}^i, \mathbf{c})}{p_{\theta_{\text{old}}}(\mathbf{x}_t^i \mid \mathbf{x}_{t-1}^i, \mathbf{c})}$ is the probability ratio and A_i is the advantage.

We decompose the clipped objective by defining indicator variables:

$$u_1 \leftarrow \mathbb{I}(\rho_{t,i} \leq 1 - \epsilon), \quad u_2 \leftarrow \mathbb{I}(\rho_{t,i} \geq 1 + \epsilon), \quad v_1 \leftarrow \mathbb{I}(A_i < 0). \quad (\text{S27})$$

The clipped objective can be rewritten as:

$$\begin{aligned} \mathcal{P}(A_i, \rho_{t,i}) &= \min(\rho_{t,i} A_i, \text{clip}(\rho_{t,i}, 1 - \epsilon, 1 + \epsilon) A_i) \\ &= \begin{cases} (1 - \epsilon) A_i, & \text{if } u_1 \wedge v_1, \\ (1 + \epsilon) A_i, & \text{if } u_2 \wedge \neg v_1, \\ \rho_{t,i} A_i, & \text{otherwise.} \end{cases} \end{aligned} \quad (\text{S28})$$

The above decomposition implies that when the probability ratio deviates significantly from 1, the clipped objective suppresses updates; when it remains within the clipping bounds (the typical stable-training regime), the objective reduces to the unclipped form:

$$\nabla_\theta \mathcal{J}_{\text{GRPO}}(\theta) = \nabla_\theta \mathbb{E}_{\mathbf{c} \sim \mathcal{D}_c, \mathbf{x}_t^i \sim \pi_{\theta_{\text{old}}}(\cdot \mid \mathbf{c})} [\rho_{t,i} A_i]. \quad (\text{S29})$$

Next, applying a change of measure from $\pi_{\theta_{\text{old}}}$ to the uniform distribution \mathcal{U} yields:

$$\begin{aligned} \mathcal{J}_{\text{GRPO}}(\theta) &= \mathbb{E}_{\mathbf{c} \sim \mathcal{D}_c, \mathbf{x}_t^i \sim \pi_{\theta_{\text{old}}}(\cdot \mid \mathbf{c})} \left[A_i \frac{p_\theta(\mathbf{x}_t^i \mid \mathbf{x}_{t-1}^i, \mathbf{c})}{p_{\theta_{\text{old}}}(\mathbf{x}_t^i \mid \mathbf{x}_{t-1}^i, \mathbf{c})} \right] \\ &= \mathbb{E}_{\mathbf{c} \sim \mathcal{D}_c, \mathbf{x}_t^i \sim \mathcal{U}} \left[A_i \cdot p_{\theta_{\text{old}}}(\mathbf{x}_t^i \mid \mathbf{x}_{t-1}^i, \mathbf{c}) \cdot \frac{p_\theta(\mathbf{x}_t^i \mid \mathbf{x}_{t-1}^i, \mathbf{c})}{p_{\theta_{\text{old}}}(\mathbf{x}_t^i \mid \mathbf{x}_{t-1}^i, \mathbf{c})} \right] \\ &= \mathbb{E}_{\mathbf{c} \sim \mathcal{D}_c, \mathbf{x}_t^i \sim \mathcal{U}} [A_i \cdot p_\theta(\mathbf{x}_t^i \mid \mathbf{x}_{t-1}^i, \mathbf{c})]. \end{aligned} \quad (\text{S30})$$

Using the log-derivative trick, we obtain:

$$\nabla_\theta \log p_\theta(\mathbf{x}_t^i \mid \mathbf{x}_{t-1}^i, \mathbf{c}) = \frac{\nabla_\theta p_\theta(\mathbf{x}_t^i \mid \mathbf{x}_{t-1}^i, \mathbf{c})}{p_\theta(\mathbf{x}_t^i \mid \mathbf{x}_{t-1}^i, \mathbf{c})}, \quad (\text{S31})$$

which implies:

$$\nabla_\theta p_\theta(\mathbf{x}_t^i \mid \mathbf{x}_{t-1}^i, \mathbf{c}) = p_\theta(\mathbf{x}_t^i \mid \mathbf{x}_{t-1}^i, \mathbf{c}) \cdot \nabla_\theta \log p_\theta(\mathbf{x}_t^i \mid \mathbf{x}_{t-1}^i, \mathbf{c}). \quad (\text{S32})$$

Taking the gradient of Eq. (S30):

$$\begin{aligned} \nabla_\theta \mathcal{J}_{\text{GRPO}}(\theta) &= \mathbb{E}_{\mathbf{c} \sim \mathcal{D}_c, \mathbf{x}_t^i \sim \mathcal{U}} [A_i \cdot \nabla_\theta p_\theta(\mathbf{x}_t^i \mid \mathbf{x}_{t-1}^i, \mathbf{c})] \\ &= \mathbb{E}_{\mathbf{c} \sim \mathcal{D}_c, \mathbf{x}_t^i \sim \mathcal{U}} [A_i \cdot p_\theta(\mathbf{x}_t^i \mid \mathbf{x}_{t-1}^i, \mathbf{c}) \cdot \nabla_\theta \log p_\theta(\mathbf{x}_t^i \mid \mathbf{x}_{t-1}^i, \mathbf{c})] \\ &= \mathbb{E}_{\mathbf{c} \sim \mathcal{D}_c, \mathbf{x}_t^i \sim \pi_\theta(\mathbf{x}_t^i \mid \mathbf{x}_{t-1}^i, \mathbf{c})} [A_i \cdot \nabla_\theta \log p_\theta(\mathbf{x}_t^i \mid \mathbf{x}_{t-1}^i, \mathbf{c})]. \end{aligned} \quad (\text{S33})$$

For flow-matching models, the conditional distribution at step t is Gaussian:

$$p_\theta(\mathbf{x}_t \mid \mathbf{x}_{t-\Delta t}, \mathbf{c}) \sim \mathcal{N}(\mu_\theta(\mathbf{x}_t, t, \mathbf{c}); \mathbf{x}_{t-\Delta t}, \eta^2 \Delta t), \quad (\text{S34})$$

where μ_θ is the predicted mean and $\eta^2 \Delta t$ is the variance. The log-probability is:

$$\log p_\theta(\mathbf{x}_t | \mathbf{x}_{t-\Delta t}, \mathbf{c}) = -\frac{\|\mu_\theta(\mathbf{x}_t, t, \mathbf{c}) - \mathbf{x}_{t-\Delta t}\|_2^2}{2\eta^2 \Delta t} + \text{const.} \quad (\text{S35})$$

Consequently, we have:

$$\nabla_\theta \log p_\theta(\mathbf{x}_t | \mathbf{x}_{t-\Delta t}, \mathbf{c}) = -\nabla_\theta \frac{\|\mu_\theta(\mathbf{x}_t, t, \mathbf{c}) - \mathbf{x}_{t-\Delta t}\|_2^2}{2\eta^2 \Delta t}. \quad (\text{S36})$$

Plugging the above into the gradient expression in Eq. (S33), we obtain:

$$\nabla_\theta \mathcal{J}_{\text{GRPO}} = \begin{cases} 0, & \text{if } (u_1 \wedge v_1) \vee (u_2 \wedge \neg v_1), \\ \mathbb{E} \left[-\omega(t) \cdot \mathcal{A}^k \cdot \nabla_\theta \|\mu_\theta(\mathbf{x}_t, t, \mathbf{c}) - \mathbf{x}_{t-1}\|_2^2 \right], & \text{else.} \end{cases}$$

Combining the above, we recover the stated corollary form: the gradient vanishes in the clipped regions and otherwise equals the gradient of a reward- and time-weighted squared prediction error $\|\mu_\theta(\mathbf{x}_t, t, \mathbf{c}) - \mathbf{x}_{t-1}\|_2^2$, concluding the proof. \square

E.2. Corollary for DDPO & DPO

E.2.1. Corollary for DDPO

Corollary (DDPO Trajectory Imitation). Given a flow model θ , a reward model $r(\mathbf{x}, \mathbf{c})$, and trajectories sampled via SDE in Eq. (1), the gradient of DDPO satisfies:

$$\mathcal{J}_{\text{DDPO}} = \nabla_\theta \mathbb{E} \left[\omega(t) \cdot r(\mathbf{x}_0^k, \mathbf{c}) \cdot \nabla_\theta \|\mu_\theta(\mathbf{x}_t, t, \mathbf{c}) - \mathbf{x}_{t-1}\|_2^2 \right],$$

where $\mu_\theta(\cdot)$ denotes the mean of the predicted distribution $p_\theta(\mathbf{x}_t | \mathbf{x}_{t-1}, \mathbf{c})$.

Proof of DDPO Corollary. We prove that the DDPO gradient reduces to a reward-weighted trajectory imitation objective. The standard DDPO objective is:

$$\nabla_\theta \mathcal{J}_{\text{DDPO}}(\theta) = \nabla_\theta \mathbb{E}_{\mathbf{c} \sim \mathcal{D}_c, \mathbf{x}_t^k \sim \pi_{\theta_{\text{old}}}(\cdot | \mathbf{c}), t \sim \mathcal{U}(0, T), k \sim \mathcal{U}(1, K)} \left[\frac{p_\theta(\mathbf{x}_t^k | \mathbf{x}_{t-1}^k)}{p_{\theta_{\text{old}}}(\mathbf{x}_t^k | \mathbf{x}_{t-1}^k)} \cdot r(\mathbf{x}_0^k, \mathbf{c}) \cdot \log p_\theta(\mathbf{x}_t^k | \mathbf{x}_{t-1}^k, \mathbf{c}) \right]. \quad (\text{S37})$$

From importance sampling, we derive the following gradient:

$$\begin{aligned} \nabla_\theta \mathcal{J}_{\text{DDPO}}(\theta) &= \mathbb{E}_{\mathbf{c} \sim \mathcal{D}_c} [r(\mathbf{x}_0^k, \mathbf{c}) \cdot p_\theta(\mathbf{x}_t^k) \cdot \nabla_\theta \log p_\theta(\mathbf{x}_t^k | \mathbf{x}_{t-1}^k, \mathbf{c})] \\ &= \mathbb{E}_{\mathbf{c} \sim \mathcal{D}_c, \mathbf{x}_t^k \sim \pi_\theta(\cdot | \mathbf{c})} [r(\mathbf{x}_0^k, \mathbf{c}) \cdot \nabla_\theta \log p_\theta(\mathbf{x}_t^k | \mathbf{x}_{t-1}^k, \mathbf{c})] \end{aligned} \quad (\text{S38})$$

For flow-matching models, the conditional distribution at step t is Gaussian:

$$p_\theta(\mathbf{x}_t | \mathbf{x}_{t-1}, \mathbf{c}) \sim \mathcal{N}(\mu_\theta(\mathbf{x}_t, t, \mathbf{c}); \mathbf{x}_{t-1}, \eta^2 \Delta t), \quad (\text{S39})$$

where μ_θ is the predicted mean and $\eta^2 \Delta t$ is the variance. The log-probability is:

$$\log p_\theta(\mathbf{x}_t | \mathbf{x}_{t-1}, \mathbf{c}) = -\frac{\|\mu_\theta(\mathbf{x}_t, t, \mathbf{c}) - \mathbf{x}_{t-1}\|_2^2}{2\eta^2 \Delta t} + \text{const.} \quad (\text{S40})$$

Consequently:

$$\nabla_\theta \log p_\theta(\mathbf{x}_t | \mathbf{x}_{t-1}, \mathbf{c}) = -\nabla_\theta \frac{\|\mu_\theta(\mathbf{x}_t, t, \mathbf{c}) - \mathbf{x}_{t-1}\|_2^2}{2\eta^2 \Delta t}. \quad (\text{S41})$$

Plugging this into Eq. (S38):

$$\nabla_\theta \mathcal{J}_{\text{DDPO}}(\theta) = \mathbb{E}_{\mathbf{c} \sim \mathcal{D}_c, \mathbf{x}_t^k \sim \pi_\theta(\cdot | \mathbf{c})} \left[r(\mathbf{x}_0^k, \mathbf{c}) \cdot \left(-\nabla_\theta \frac{\|\mu_\theta(\mathbf{x}_t, t, \mathbf{c}) - \mathbf{x}_{t-1}\|_2^2}{2\eta^2 \Delta t} \right) \right]. \quad (\text{S42})$$

This establishes that DDPO reduces to reward-weighted trajectory imitation, where the model learns to imitate high-reward trajectories. \square

E.2.2. Corollary for DPO

Corollary (DPO Trajectory Imitation). Given a flow model θ , a reference model θ_{ref} , and preference pairs $(\mathbf{x}^1, \mathbf{x}^2)$ where $\mathbf{x}^1 \succ \mathbf{x}^2$ sampled via SDE in Eq. (1), the gradient of DPO satisfies

$$\nabla_{\theta} \mathcal{J}_{\text{DPO}}(\theta) = \mathbb{E} \left[(1 - \sigma(m_t)) \cdot \left(-\omega(t) \nabla_{\theta} \left(\|\mu_{\theta}(\mathbf{x}_t^1, t, \mathbf{c}) - \mathbf{x}_{t-1}^1\|_2^2 - \|\mu_{\theta}(\mathbf{x}_t^2, t, \mathbf{c}) - \mathbf{x}_{t-1}^2\|_2^2 \right) \right) \right]$$

where

$$m_t = \beta \log \frac{p_{\theta}(\mathbf{x}_t^1 \mid \mathbf{x}_{t-1}^1, c)}{p_{\theta_{\text{ref}}}(\mathbf{x}_t^1 \mid \mathbf{x}_{t-1}^1, c)} - \beta \log \frac{p_{\theta}(\mathbf{x}_t^2 \mid \mathbf{x}_{t-1}^2, c)}{p_{\theta_{\text{ref}}}(\mathbf{x}_t^2 \mid \mathbf{x}_{t-1}^2, c)}$$

denotes the per-timestep preference margin, $\beta > 0$ is the temperature parameter, and $\omega(t) > 0$ is a constant that depends only on β and the Gaussian variance (e.g., $\omega(t) = \frac{\beta}{2\eta^2\Delta t}$ under the parameterization in Eq. (S40)) but is independent of θ .

Proof of DPO Corollary. The DPO objective for preference pairs is:

$$\mathcal{J}_{\text{DPO}}(\theta) = \mathbb{E}_{c \sim \mathcal{D}, \mathbf{x}^1 \succ \mathbf{x}^2, t \sim \mathcal{U}(0, T)} \left[\log \sigma \left(\beta \log \frac{p_{\theta}(\mathbf{x}_t^1 \mid \mathbf{x}_{t-1}^1, c)}{p_{\theta_{\text{ref}}}(\mathbf{x}_t^1 \mid \mathbf{x}_{t-1}^1, c)} - \beta \log \frac{p_{\theta}(\mathbf{x}_t^2 \mid \mathbf{x}_{t-1}^2, c)}{p_{\theta_{\text{ref}}}(\mathbf{x}_t^2 \mid \mathbf{x}_{t-1}^2, c)} \right) \right]. \quad (\text{S43})$$

Define the per-timestep preference margin

$$m_t := \beta \log \frac{p_{\theta}(\mathbf{x}_t^1 \mid \mathbf{x}_{t-1}^1, c)}{p_{\theta_{\text{ref}}}(\mathbf{x}_t^1 \mid \mathbf{x}_{t-1}^1, c)} - \beta \log \frac{p_{\theta}(\mathbf{x}_t^2 \mid \mathbf{x}_{t-1}^2, c)}{p_{\theta_{\text{ref}}}(\mathbf{x}_t^2 \mid \mathbf{x}_{t-1}^2, c)}, \quad (\text{S44})$$

so that $\mathcal{J}_{\text{DPO}}(\theta) = \mathbb{E}[\log \sigma(m_t)]$. Taking the gradient and applying the chain rule with the sigmoid derivative $\sigma'(z) = \sigma(z)(1 - \sigma(z))$ yields

$$\nabla_{\theta} \mathcal{J}_{\text{DPO}}(\theta) = \mathbb{E}[(1 - \sigma(m_t)) \cdot \nabla_{\theta} m_t]. \quad (\text{S45})$$

Next, we express m_t in terms of the Gaussian likelihoods used by the flow model. For flow-matching models, the conditional distribution at step t is Gaussian with variance $\eta^2\Delta t$:

$$p_{\theta}(\mathbf{x}_t \mid \mathbf{x}_{t-1}, \mathbf{c}) \sim \mathcal{N}(\mu_{\theta}(\mathbf{x}_t, t, \mathbf{c}); \mathbf{x}_{t-1}, \eta^2\Delta t), \quad (\text{S46})$$

so that

$$\log p_{\theta}(\mathbf{x}_t \mid \mathbf{x}_{t-1}, \mathbf{c}) = -\frac{\|\mu_{\theta}(\mathbf{x}_t, t, \mathbf{c}) - \mathbf{x}_{t-1}\|_2^2}{2\eta^2\Delta t} + \text{const.} \quad (\text{S47})$$

where the constant does not depend on θ . Since the reference model θ_{ref} is fixed, its log-likelihood terms are constant with respect to θ and vanish under ∇_{θ} . Consequently, the contribution of the reference model θ_{ref} to the margin m_t is a constant with respect to θ , and thus plays no role in the gradient. Therefore, up to an additive constant independent of θ , we have

$$m_t = -\frac{\beta}{2\eta^2\Delta t} \left(\|\mu_{\theta}(\mathbf{x}_t^1, t, \mathbf{c}) - \mathbf{x}_{t-1}^1\|_2^2 - \|\mu_{\theta}(\mathbf{x}_t^2, t, \mathbf{c}) - \mathbf{x}_{t-1}^2\|_2^2 \right) + \text{const.} \quad (\text{S48})$$

Taking the gradient with respect to θ gives

$$\nabla_{\theta} m_t = -\frac{\beta}{2\eta^2\Delta t} \nabla_{\theta} \left(\|\mu_{\theta}(\mathbf{x}_t^1, t, \mathbf{c}) - \mathbf{x}_{t-1}^1\|_2^2 - \|\mu_{\theta}(\mathbf{x}_t^2, t, \mathbf{c}) - \mathbf{x}_{t-1}^2\|_2^2 \right). \quad (\text{S49})$$

Substituting this expression into Eq. (S45) and defining $\omega(t) := \frac{\beta}{2\eta^2\Delta t} > 0$, we obtain

$$\nabla_{\theta} \mathcal{J}_{\text{DPO}}(\theta) = \mathbb{E} \left[(1 - \sigma(m_t)) \cdot \left(-\omega(t) \nabla_{\theta} \left(\|\mu_{\theta}(\mathbf{x}_t^1, t, \mathbf{c}) - \mathbf{x}_{t-1}^1\|_2^2 - \|\mu_{\theta}(\mathbf{x}_t^2, t, \mathbf{c}) - \mathbf{x}_{t-1}^2\|_2^2 \right) \right) \right] \quad (\text{S50})$$

The proof is completed. \square

This shows that maximizing the DPO objective is equivalent (up to the positive scalar factor $\omega(t)$) to minimizing a preference-weighted trajectory imitation loss, in which the model is encouraged to decrease the prediction error along preferred trajectories and increase it along dispreferred trajectories, with weights given by $(1 - \sigma(m_t))$ that depend on the current preference margin.

E.3. Theoretical Justification for CPGO

We provide theoretical justification for CPGO by establishing a connection to consistency models [50]. The key insight is that minimizing the CPGO objective encourages the current model to maintain consistency with the previous model across the denoising trajectory, which in turn controls the accumulated error in multi-step ODE integration.

Notation. For brevity, we denote $\pi_\theta(\mathbf{x}, t) := \pi_\theta^{\text{ODE}}(\mathbf{x}, t)$ as the ODE-based single-step prediction function, and omit the sample index k when clear from context. We use \mathbf{x}_{t_n} to denote the state at discrete time step t_n in the trajectory.

Theorem S1 (Consistency Property of Flow Models). *Let $\Delta t := \max_{n \in [1, T-1]} \{|t_{n+1} - t_n|\}$ denote the maximum time step size, and π_θ satisfy the following assumptions:*

1. *π_θ is Lipschitz continuous in \mathbf{x} with constant $L > 0$: $\|\pi_\theta(\mathbf{x}, t) - \pi_\theta(\mathbf{y}, t)\|_2 \leq L\|\mathbf{x} - \mathbf{y}\|_2$.*
2. *The boundary condition is satisfied: $\pi_\theta(\mathbf{x}, 0) = \mathbf{x}$.*
3. *The ODE solver has local truncation error $O((t_{n+1} - t_n)^{p+1})$ for some $p \geq 1$.*

If $\mathcal{J}_{\text{CPGO}}(\theta, \mathcal{G}) = 0$, then the prediction error between the current and old models satisfies:

$$\sup_{n, \mathbf{x}} \|\pi_\theta(\mathbf{x}, t_n) - \pi_{\theta_{\text{old}}}(\mathbf{x}, t_n)\|_2 = O((\Delta t)^{p+1}).$$

Proof of Theorem S1. The CPGO objective is defined as:

$$\mathcal{J}_{\text{CPGO}}(\theta, \mathcal{G}) = \mathbb{E}_{\mathbf{x}_t \sim \mathcal{G}} [\|\pi_\theta(\mathbf{x}_t, t) - \pi_{\theta_{\text{old}}}(\mathbf{x}_{t-1}, t-1)\|_2^2], \quad (\text{S51})$$

where \mathbf{x}_{t-1} is the predecessor state in the trajectory. When $\mathcal{J}_{\text{CPGO}}(\theta, \mathcal{G}) = 0$, we have:

$$\mathbb{E}_{\mathbf{x}_t, \mathbf{x}_{t-1}} [\|\pi_\theta(\mathbf{x}_t, t) - \pi_{\theta_{\text{old}}}(\mathbf{x}_{t-1}, t-1)\|_2^2] = 0. \quad (\text{S52})$$

Since the integrand is non-negative and its expectation is zero, the integrand must vanish almost everywhere over the support of the joint distribution $p(\mathbf{x}_t, \mathbf{x}_{t-1})$:

$$\|\pi_\theta(\mathbf{x}_t, t) - \pi_{\theta_{\text{old}}}(\mathbf{x}_{t-1}, t-1)\|_2 = 0. \quad (\text{S53})$$

For a trajectory $\{\mathbf{x}_{t_n}\}_{n=0}^T$ generated by the old model, the consistency condition (Eq. (S53)) implies that at each step n :

$$\pi_\theta(\mathbf{x}_{t_n}, t_n) = \pi_{\theta_{\text{old}}}(\mathbf{x}_{t_{n-1}}, t_{n-1}) \quad (\text{S54})$$

This means the current model's prediction at (\mathbf{x}_{t_n}, t_n) matches the old model's prediction at the previous step $(\mathbf{x}_{t_{n-1}}, t_{n-1})$. Rearranging:

$$\pi_\theta(\mathbf{x}_{t_n}, t_n) - \pi_{\theta_{\text{old}}}(\mathbf{x}_{t_n}, t_n) = \pi_{\theta_{\text{old}}}(\mathbf{x}_{t_{n-1}}, t_{n-1}) - \pi_{\theta_{\text{old}}}(\mathbf{x}_{t_n}, t_n). \quad (\text{S55})$$

The right-hand side of Eq. (S55) represents the single-step ODE integration error of the old model. By Assumption 3, the ODE solver has local truncation error $O((t_{n+1} - t_n)^{p+1})$. For a p -th order method applied to the ODE $\frac{d\mathbf{x}}{dt} = v_{\theta_{\text{old}}}(\mathbf{x}, t)$, the single-step error satisfies:

$$\|\pi_{\theta_{\text{old}}}(\mathbf{x}_{t_{n-1}}, t_{n-1}) - \pi_{\theta_{\text{old}}}(\mathbf{x}_{t_n}, t_n)\|_2 = O((t_n - t_{n-1})^{p+1}). \quad (\text{S56})$$

By the Lipschitz assumption on π_θ (Assumption 1), we can bound the model disagreement:

$$\begin{aligned} \|\pi_\theta(\mathbf{x}_{t_n}, t_n) - \pi_{\theta_{\text{old}}}(\mathbf{x}_{t_n}, t_n)\|_2 &\leq \|\pi_{\theta_{\text{old}}}(\mathbf{x}_{t_{n-1}}, t_{n-1}) - \pi_{\theta_{\text{old}}}(\mathbf{x}_{t_n}, t_n)\|_2 \\ &= O((t_n - t_{n-1})^{p+1}) \leq O((\Delta t)^{p+1}). \end{aligned} \quad (\text{S57})$$

Taking the supremum over all time steps and states:

$$\sup_{n, \mathbf{x}} \|\pi_\theta(\mathbf{x}_{t_n}, t_n) - \pi_{\theta_{\text{old}}}(\mathbf{x}_{t_n}, t_n)\|_2 = O((\Delta t)^{p+1}). \quad (\text{S58})$$

This bound shows that when CPGO is minimized, the prediction error between the current and old models is controlled by the ODE discretization error, which decays as $O((\Delta t)^{p+1})$ with finer time steps. The proof is completed. \square

F. Visualization

Here, we provide visualizations corresponding to the additional experimental results reported in Sec. A.

Prompt: A Wojak looking over a sea of memes from a cliff on 4chan.



(a) Grid Pattern

Prompt: A cat in a tutu dancing to Swan Lake.



(c) Semantic Misalignment



Prompt: A raccoon riding an oversized fox through a forest in a furry art anime still.



(b) Irrelevant Details



Prompt: The image depicts a ... a colossal, ancient ruin with a road winding through the forest, overlooking a sunrise above the cloudy sea.



(d) Detail Over-Optimization

Fine-Grained Optimization (From Left to Right)

Prompt: The image depicts three female figures playing musical instruments.



(e) Local Details Overlook

Prompt: A young woman sitting on the floor, relaxed pose, casual outfit with leather boots, warm and clean aesthetic.



**(f) Convergence Difficulty
(Due to Repeated Coarse-Grained Exploration)**

Prompt: A still of Doraemon from "Shaun the Sheep" by Aardman Animation.



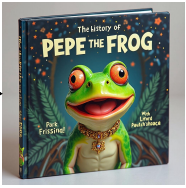
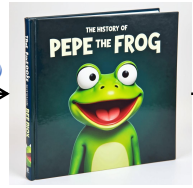
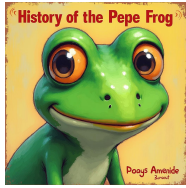
Prompt: A raccoon riding an oversized fox through a forest in a furry art anime still.



(g) Blurred Image (Maybe Caused by Overly Diverse and Even Ambiguous Coarse-Grained Exploration)

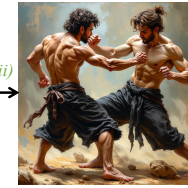
Coarse-Grained Optimization (From Left to Right)

Prompt: A book about the history of Pepe the Frog.



(i) Coarse-Grained Optimization for Global Semantics

Prompt: A painting featuring two men in a fighting scene.



(ii) Fine-Grained Optimization for Local Details

Dynastic-Grained Optimization (From Left to Right)

Figure S9. Qualitative comparison of coarse-, fine-, and dynamic-grained optimization strategies. Fine-grained optimization achieves sharp details but suffers from over-sharpening and detail accumulation artifacts. Coarse-grained optimization maintains semantic diversity but may lack fine details. Our dynamic-grained approach balances both, combining the strengths of each strategy to achieve visually superior results with fewer hallucination artifacts.



Original image of the grid pattern

Enhanced image to better reveal the grid pattern



Semantics Misalignment
& Details Over-Optimization

Irrelevant Details

Details Over-Optimization

Figure S10. Enlarged view of Fig. 1 from the Sec. Introduction. This enlarged visualization is provided to allow readers to more clearly observe fine-grained details and visual hallucination artifacts, including detail over-sharpening, irrelevant detail accumulation, and grid pattern artifacts discussed in the paper. *These results are reproduced using official model weights or implementation settings of existing methods, with 8 GPUs.*

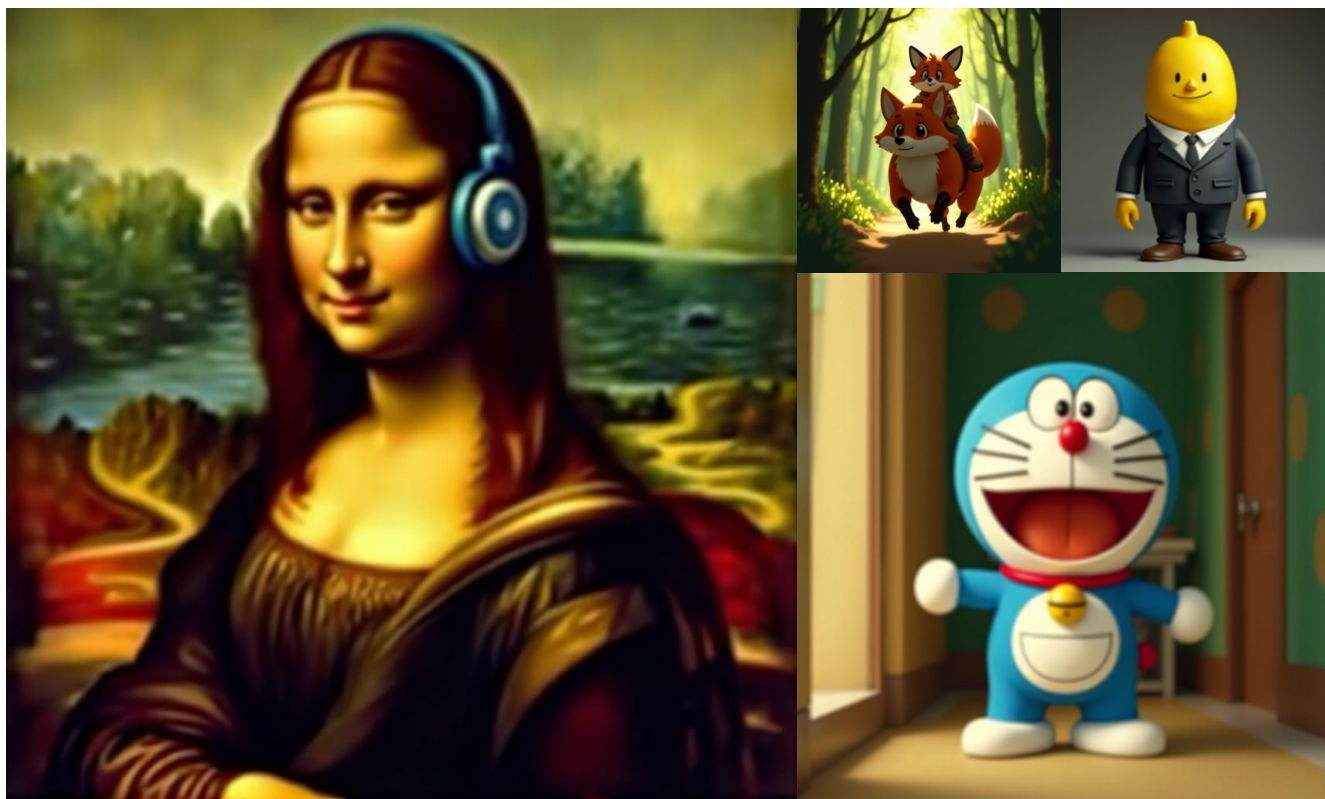


Figure S11. Enlarged view of blurred image. *These results are reproduced using official model weights or implementation settings of existing methods, with 8 GPUs.*